



ARL-TR-7927 • JAN 2017



# **Polymeric Materials Models in the Warrior Injury Assessment Manikin (WIAMan) Anthropomorphic Test Device (ATD) Tech Demonstrator**

**by M Chowdhury, D Crawford, M Shanaman, M Boyle,  
R Armiger, C Bell, K Lister, and A Shirley**

Approved for public release; distribution unlimited.

## **NOTICES**

### **Disclaimers**

The findings in this report are not to be construed as an official Department of the Army position unless so designated by other authorized documents.

Citation of manufacturer's or trade names does not constitute an official endorsement or approval of the use thereof.

Destroy this report when it is no longer needed. Do not return it to the originator.



# **Polymeric Materials Models in the Warrior Injury Assessment Manikin (WIAMan) Anthropomorphic Test Device (ATD) Tech Demonstrator**

**by M Chowdhury and D Crawford**

*Weapons and Materials Research Directorate, ARL*

**M Shanaman, M Boyle, and R Armiger**

*Johns Hopkins Applied Physics Lab, Laurel, MD*

**C Bell, K Lister, and A Shirley**

*Corvid Technologies, Mooresville, NC*

REPORT DOCUMENTATION PAGE				Form Approved OMB No. 0704-0188	
<p>Public reporting burden for this collection of information is estimated to average 1 hour per response, including the time for reviewing instructions, searching existing data sources, gathering and maintaining the data needed, and completing and reviewing the collection information. Send comments regarding this burden estimate or any other aspect of this collection of information, including suggestions for reducing the burden, to Department of Defense, Washington Headquarters Services, Directorate for Information Operations and Reports (0704-0188), 1215 Jefferson Davis Highway, Suite 1204, Arlington, VA 22202-4302. Respondents should be aware that notwithstanding any other provision of law, no person shall be subject to any penalty for failing to comply with a collection of information if it does not display a currently valid OMB control number.</p> <p><b>PLEASE DO NOT RETURN YOUR FORM TO THE ABOVE ADDRESS.</b></p>					
1. REPORT DATE (DD-MM-YYYY) January 2017		2. REPORT TYPE Technical Report		3. DATES COVERED (From - To) 06/2015 to 09/2016	
4. TITLE AND SUBTITLE Polymeric Materials Models in the Warrior Injury Assessment Manikin (WIAMan) Anthropomorphic Test Device (ATD) Tech Demonstrator				5a. CONTRACT NUMBER	
				5b. GRANT NUMBER	
				5c. PROGRAM ELEMENT NUMBER	
6. AUTHOR(S) M Chowdhury, D Crawford, M Shanaman, M Boyle, R Armiger, C Bell, K Lister, and A Shirley				5d. PROJECT NUMBER	
				5e. TASK NUMBER	
				5f. WORK UNIT NUMBER	
7. PERFORMING ORGANIZATION NAME(S) AND ADDRESS(ES) US Army Research Laboratory ATTN: RDRL-DPW Aberdeen Proving Ground, MD 21005				8. PERFORMING ORGANIZATION REPORT NUMBER  ARL-TR-7927	
9. SPONSORING/MONITORING AGENCY NAME(S) AND ADDRESS(ES)				10. SPONSOR/MONITOR'S ACRONYM(S)	
				11. SPONSOR/MONITOR'S REPORT NUMBER(S)	
12. DISTRIBUTION/AVAILABILITY STATEMENT Approved for public release; distribution unlimited.					
13. SUPPLEMENTARY NOTES					
14. ABSTRACT The Warrior Injury Assessment Manikin (WIAMan) Engineering Office has been developing a biofidelic anthropomorphic test device (ATD) to enable the live-fire test and evaluation community to address the deficiencies associated with the use of the Hybrid III ATD to assess the risk of mounted-Soldier injuries subjected to under-body blast. A finite-element (FE) virtual modeling tool has been developed to support the design and development of the WIAMan ATD. Material characterization is one of the critical challenges facing the ATD modeling community because of the lack of adequate material models and inconsistency between material models available in different FE codes. The WIAMan modeling and simulation team systematically characterized the material properties using experimental data for 8 polymeric materials used in key components in the WIAMan ATD Tech Demonstrator. Two modeling teams independently simulated the WIAMan ATD in vertical accelerative loading simulations using 2 different modeling platforms (LS-DYNA and Velodyne). The approaches to derive the material parameters, constitutive material models, and the fitting algorithms are discussed in this report. A brief summary of the whole-body simulation results of an ATD response due to vertical accelerative loading is provided and compared to illustrate the predictive capability of the derived material models.					
15. SUBJECT TERMS under-body blast, finite-element model, Warrior Injury Assessment Manikin, WIAMan ATD, anthropomorphic test device, validation					
16. SECURITY CLASSIFICATION OF:			17. LIMITATION OF ABSTRACT  UU	18. NUMBER OF PAGES  66	19a. NAME OF RESPONSIBLE PERSON M Chowdhury
a. REPORT Unclassified	b. ABSTRACT Unclassified	c. THIS PAGE Unclassified			19b. TELEPHONE NUMBER (Include area code) (301) 394-2917

## Contents

---

<b>List of Figures</b>	<b>v</b>
<b>List of Tables</b>	<b>vii</b>
<b>1. Introduction</b>	<b>1</b>
<b>2. WIAMan Material Description and Material Test Data</b>	<b>4</b>
2.1 WIAMan Material Description	4
2.2 WIAMan Material Test Data	4
<b>3. Velodyne Material Models</b>	<b>6</b>
3.1 Parameterization Procedure	7
3.2 Results for Velodyne Materials Models	14
3.2.1 Proflex 30 Pelvis Flesh	15
3.2.2 XE1031 Foot Flesh	16
3.2.3 FD70 Foot Plate	17
3.2.4 Delrin Calcaneus Cap	18
3.2.5 E1030AL Flesh (Other)	19
3.2.6 Butyl Rubber (75 Shore A) Compliant Elements	20
3.2.7 Rencast 6425 Tailbone	21
3.2.8 TC892 Pelvis Bone	22
<b>4. LS-DYNA Material Models</b>	<b>23</b>
4.1 Polymer Material Models	24
4.1.1 *MAT_OGDEN_RUBBER	24
4.1.2 *MAT_BERGSTROM_BOYCE_RUBBER	25
4.1.3 *MAT_SIMPLIFIED_JOHNSON_COOK	26
4.1.4 *MAT_BLATZ-KO_RUBBER	27
4.2 Polymer Fitting Procedure	27
4.2.1 MCalibration Software	30
4.2.2 LS-OPT Software	31
4.2.3 Molded Neck Rubber Fit Procedure	31
4.3 Polymer Fitting Results	32

4.3.1	Butyl Rubber 75 Shore A Compliant Elements and Spine Rubber	32
4.3.2	Proflex 30 Polyurethane Pelvis Flesh	33
4.3.3	E1030AL Polyurethane Arm, Leg, and Abdomen Flesh	34
4.3.4	XE1031 Polyurethane Foot Flesh	35
4.3.5	FD70 Polyurethane Foot Plate	36
4.3.6	Delrin Calcaneus Cap	37
4.3.7	TC892 Polyurethane Pelvic Bone	38
4.3.8	Rencast 6425 Polyurethane Tailbone	39
4.3.9	ISODAMP Heel Plug	40
<b>5.</b>	<b>Typical WIAMan Strain Rate Environment</b>	<b>41</b>
<b>6.</b>	<b>Whole-Body ATD Model Simulation Results</b>	<b>44</b>
<b>7.</b>	<b>Conclusions</b>	<b>50</b>
<b>8.</b>	<b>References</b>	<b>52</b>
	<b>List of Symbols, Abbreviations, and Acronyms</b>	<b>55</b>
	<b>Distribution List</b>	<b>56</b>

## List of Figures

Fig. 1	Manikin FEM development timelines: historical perspective .....	2
Fig. 2	WIAMan ATD TD polymeric material definition.....	4
Fig. 3	Veryst stress-strain results at 0.1/s strain rate .....	8
Fig. 4	The Veryst Proflex 30 compression material test specimen (left) and the FE mesh counterpart (right) .....	8
Fig. 5	Velodyne schematic for the Veryst compression testing.....	9
Fig. 6	Process flow for inverse analysis using DAKOTA to iterate parallel runs of Velodyne .....	12
Fig. 7	Comparison of the Ogden viscoelastic model to experimental compression data for the Proflex 30 pelvis flesh.....	15
Fig. 8	Comparison of the Ogden viscoelastic model to experimental compression data for the XE1031 foot flesh.....	16
Fig. 9	Comparison of the Ogden viscoelastic model to experimental compression data for the FD70 foot plate.....	17
Fig. 10	Comparison of the Ogden viscoelastic model to experimental compression data for the Delrin calcaneus cap.....	18
Fig. 11	Comparison of the Ogden viscoelastic model to experimental compression data for the E1030AL flesh.....	19
Fig. 12	Comparison of the Ogden viscoelastic model to experimental compression data for the butyl rubber 75A.....	20
Fig. 13	Comparison of the Ogden viscoelastic model to experimental compression data for the Rencast 6425 tailbone.....	21
Fig. 14	Comparison of the Ogden viscoelastic model to experimental compression data for the TC892 pelvis bone.....	22
Fig. 15	BB fit for butyl rubber (top) vs. Ogden+Prony fit (bottom) at strain rates of 1 s <sup>-1</sup> (red) and 50 s <sup>-1</sup> (green) .....	28
Fig. 16	Performance results of the tibia and calcaneus load cells during SoD and WH1a load cases using different foot flesh material models.....	29
Fig. 17	Butyl rubber 75 Shore A material fit .....	33
Fig. 18	Pelvis flesh material fit .....	34
Fig. 19	Arm, leg, and abdomen flesh material fit .....	35
Fig. 20	Foot flesh material fit.....	36
Fig. 21	Foot plate material fit.....	37
Fig. 22	Calcaneus cap material fit.....	38
Fig. 23	Pelvis bone material fit .....	39
Fig. 24	Tailbone material fit.....	40

Fig. 25	Heel plug material fit .....	41
Fig. 26	Strain rates experienced by soft polymers during the VALTS test at WH1a levels (4 m/s at a 5-ms TTP floor, and seat, no PPE).....	42
Fig. 27	Strain rates experienced by soft polymers during the VALTS test at WH2a levels (6 m/s at a 5-ms TTP floor, 4 m/s at a 10-ms TTP seat, no PPE) .....	43
Fig. 28	Strain rates experienced by soft polymers during the VALTS test at WH2b levels (6 m/s at a 5-ms TTP floor, 4 m/s at a 10-ms TTP seat, with PPE) .....	43
Fig. 29	Velocity history from the WH1A and WH2A VALTS tests that are employed as the simulation boundary conditions .....	45
Fig. 30	Match pair validation results for the lower extremity at the heel and mid-tibia sensor regions for the simulation and the experiment under the WH1a test condition.....	46
Fig. 31	Match pair validation results for the lower and upper neck sensor regions for the simulation and the experiment under the WH1a test condition .....	46
Fig. 32	Match pair validation results for the lower extremity at the femur and tailbone sensor regions for the simulation and the experiment under the WH1a test condition .....	47
Fig. 33	Example cross-plots of the Velodyne simulation and test for WH1A (neck calcaneus and tibia).....	48
Fig. 34	Example cross-plots of the Velodyne simulation and test for WH1A (femur and tailbone).....	49



## List of Tables

Table 1	Veryst engineering materials tests analyses summary .....	6
Table 2	Veryst material tests.....	7
Table 3	Hyperelastic fit parameters for the Proflex 30 pelvis flesh.....	15
Table 4	Viscous fit parameters for the Proflex 30 pelvis flesh.....	15
Table 5	Hyperelastic fit parameters for the XE1031 foot flesh .....	16
Table 6	Viscous fit parameters for the XE1031 foot flesh .....	16
Table 7	Hyperelastic fit parameters for the FD70 foot plate .....	17
Table 8	Viscous fit parameters for the FD70 foot plate.....	17
Table 9	Hyperelastic fit parameters for the Delrin calcaneus cap .....	18
Table 10	Viscous fit parameters for the Delrin calcaneus cap.....	18
Table 11	Hyperelastic fit parameters for the E1030AL flesh .....	19
Table 12	Viscous fit parameters for the E1030AL flesh .....	19
Table 13	Hyperelastic fit parameters for the butyl rubber 75A .....	20
Table 14	Viscous fit parameters for the butyl rubber 75A .....	20
Table 15	Hyperelastic fit parameters for the Rencast 6425 tailbone .....	21
Table 16	Viscous fit parameters for the Rencast 6425 tailbone .....	21
Table 17	Hyperelastic fit parameters for the TC892 pelvis bone .....	22
Table 18	Viscous fit parameters for the TC892 pelvis bone.....	22
Table 19	WIAMan LS-DYNA polymer materials.....	23
Table 20	Blatz-Ko fit parameters for select WIAMan polymers.....	32
Table 21	Butyl rubber 75 Shore A material parameters .....	32
Table 22	Pelvis flesh material parameters .....	33
Table 23	Arm, leg, and abdomen flesh material parameters .....	34
Table 24	Foot flesh material parameters.....	35
Table 25	Foot plate material parameters.....	36
Table 26	Calcaneus cap material parameters .....	37
Table 27	Pelvis bone material parameters .....	38
Table 28	Tailbone material parameters.....	39
Table 29	Heel plug material parameters .....	40
Table 30	CORA summary table for the WIAMan TD WH1A Velodyne simulations .....	50

INTENTIONALLY LEFT BLANK.

## 1. Introduction

---

Historically, the live-fire test and evaluation (LFT&E) community has employed Hybrid III physical manikins for vehicle survivability and occupant safety assessment.<sup>1</sup> The Near-Term Under-Body Blast (N-T UBB) and Under-Body Blast (UBB) Methodology programs are also using a Hybrid III anthropomorphic test device (ATD) analytical model to analyze and understand the effects of blasts on vehicles.<sup>2</sup> The Hybrid III analytical model currently used by military vehicle analysts has been continuously updated to address the model's inherent deficiencies and make the simulated model's behavior more compatible for measuring occupant responses in a vertical accelerative loads associated with UBB.<sup>2</sup> The Hybrid III, in its best form (originally intended for automotive crash safety), is inadequate, has usability issues, and lacks the biofidelity to determine the risk of vehicle-mounted occupant injury in an UBB environment.<sup>2-4</sup> The Warrior Injury Assessment Manikin (WIAMan) Engineering Office (EO), sponsored by the Director, Operational Test and Evaluation (DOT&E), and executed by the Army, has been developing a biofidelic ATD to enable the LFT&E community to address the deficiencies associated with the use of the Hybrid III ATD and assess the injury risk to mounted Soldiers subjected to UBB.<sup>5</sup>

The WIAMan EO, positively encouraged by the ATD modeling community recommendations,<sup>2,4</sup> initiated a modeling and simulation (M&S) effort to develop an analytical tool to predict the response of the ATD to vertical accelerative loading. The analytical finite-element model (FEM) provided a virtual tool for the WIAMan EO to support ongoing ATD design development iterations to achieve strength-of-design, biofidelity, and usability requirements.<sup>6,7</sup> A general overview of the FEM development methods is available in the literature.<sup>8,9</sup> System-level whole-body model validation was based on paired experimental tests run on the Johns Hopkins University Applied Physics Laboratory (JHU-APL) Vertically Accelerated Load Transfer System (VALTS). The VALTS is a vertical impact simulator that allows laboratory test simulation of vertical accelerative loading of various UBB loading profiles and scenarios.<sup>10</sup> Two independent solver platforms (LS-DYNA and Velodyne) have been employed in parallel across 2 teams to model the WIAMan ATD. Combined, these 2 FEMs provided an opportunity to cross check predictability and complement weakest link, thus increasing confidence in the models' predictive capability. A competitive environment dominated the entire model development phase that drove the modelers to expedite the whole-body model development process at an unprecedented rate (see the historical perspective presented in Fig. 1).

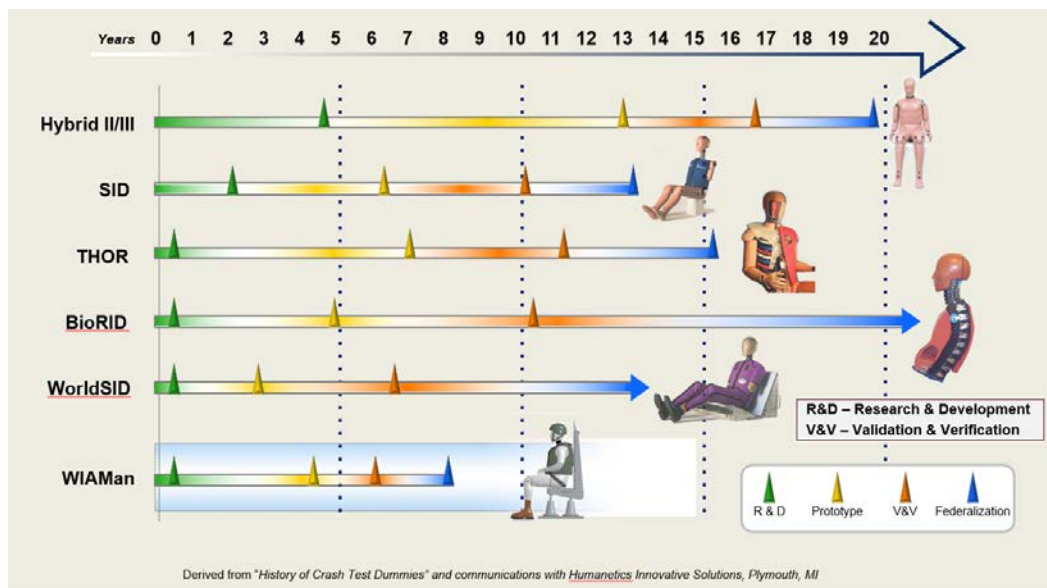


**Fig. 1 Manikin FEM development timelines: historical perspective**

The WIAMan M&S team was commissioned in August 2014 and, in a relatively short 18-month period, a functional and validated FEM of the Tech Demonstrator (TD) was developed to support the design development of the ATD. The WIAMan M&S team has been supporting the Generation (Gen) 1 (and anticipates to support Gen 2) phase of the ATD development and they are planning to produce a validated and verified (V&V) FEM of the production WIAMan ATD in a relatively shorter time period than many other manikin development timelines (see Fig 1). Rapid progress in the WIAMan ATD model development cycle was essential to inform a demanding, ongoing ATD design effort, particularly during the critical design development phase. Additionally, WIAMan EO's farsightedness in characterizing various ATD polymeric materials early in the project cycle contributed immensely in the model development process.

The success of an FEM depends primarily upon the model's ability to predict the necessary physics and interactions of the simulated environment. A simulated environment can be summed up in 3 categories: 1) initial conditions (ATD posture and rig setup), 2) boundary conditions (input velocity and rig constraints like belts), and 3) mechanical system consisting of materials and mechanism (geometry). For example, in vertical acceleration testing of a seated manikin within the VALTS environment, the vertical impactor that drives the seated ATD provides the input to the ATD, the supporting mechanisms that restrain the ATD are the boundary conditions, and the ATD itself is the mechanical system. A proper representation of the initial conditions, the input force that drives the simulated environment, the boundary conditions that define how the system is driven or acted upon by external

means (forces), and the material systems and mechanisms that constitute the model are the primary factors that govern a model's predictive capability. Among the 3 factors, material characterization is the single most critical challenge facing the ATD modeling community because of the lack of adequate material models and inconsistency among material models available in different FE codes.<sup>4,11</sup> The WIAMan M&S effort arguably addressed these 2 critical ATD modeling challenges in its undertakings. The WIAMan M&S used experimentally derived material data to construct material models, and 2 modeling teams independently simulated the WIAMan ATD vertical accelerative loaded simulations in 2 different platforms (LS-DYNA and Velodyne). The other 2 factors affecting the accuracy of simulations are more or less manageable, since the input to the model is generally deterministic and the initial as well as boundary conditions can be verified in a controlled test environment.

This report documents the material characterization process to extract material model parameters specific to the 2 FEM codes (LS-DYNA and Velodyne) for 8 polymeric materials used in key components in the WIAMan ATD TD. There are multiple constitutive models in each of the FEM codes used in this effort. LS-DYNA has a variety of material models that can model polymeric materials behavior using an empirical or rational approach.<sup>12-14</sup> Velodyne has their own material models, mostly inclusive of those available in the LS-DYNA code. The constitutive material models that these 2 codes used in their numerical simulations were derived from the same experimental data. Thus, the inconsistency between the material models used by 2 different codes is of little concern, since the simulation results were compared and verified against the same set of test data with a common reference threshold. The use of 2 FEM codes in solving an identical simulation environment also provided an opportunity to test the hypothesis that vertical accelerative response simulation of an ATD is independent of solver types given that the material models are derived from the same source. The approaches to derive the material parameters, the constitutive materials models, and the fitting algorithms are discussed in the report. This report also presents the respective model parameters for both models. Finally, the whole-body simulation results of both models of an ATD response due to vertical accelerative loading are compared using identical experimental data to document the predictive capability of the material models.

## 2. WIAMan Material Description and Material Test Data

### 2.1 WIAMan Material Description

The WIAMan TD consists of metallic structural components, specifically aluminum, steel, brass, tungsten, and titanium alloys, as well as complex hyperelastic and rate-dependent polymers, elastomers, and others. The latter of these two material classes dictates the compliance of the WIAMan and generally feature strain-rate dependent properties and thus the load responses and kinematics of the system are often governed by them. For this reason, it is important to accurately capture the behavior of these materials with regard to both rate-dependence and the stress-strain relationship. A list of representative commercially available polymeric materials, along with their basic material property definitions, currently used within the WIAMan components are shown in Fig. 2. Comprehensive material property descriptions for the WIAMan TD polymers are documented by Crawford et al.<sup>15</sup>

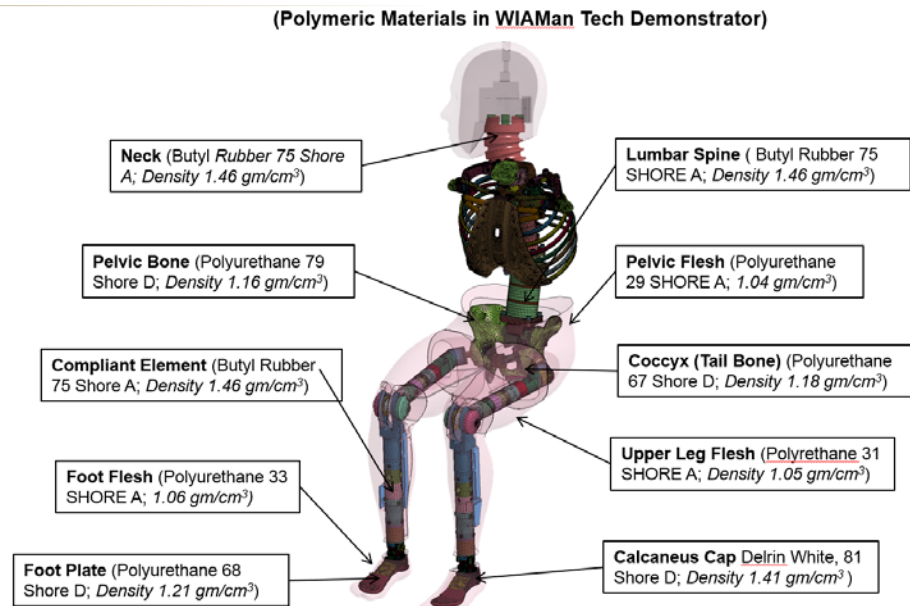


Fig. 2 WIAMan ATD TD polymeric material definition

### 2.2 WIAMan Material Test Data

Proper characterization of materials is vital to the success of an FE simulation. No simulation can serve its purpose unless the material behavior is correctly simulated. Material tests are needed to extract its behavior in different simulated environment such as tension, compression, loading, and unloading conditions. Particularly the material test data for high-strain-rate effects are important for the accelerative

vertical loading environment for which the WIAMan ATD has been designed.<sup>4</sup> An extensive materials testing program to extract material characteristics data for polymeric materials had been executed to support the WIAMan model development. Veryst Engineering LLC (Needham Heights, MA; [www.veryst.com](http://www.veryst.com)), a leading testing lab for characterization of complex nonlinear viscoelastic materials, performed the dynamic material tests for the WIAMan TD materials. Veryst Engineering designed custom test methods to capture the nonlinear, strain-rate-dependent response of the materials characterized. The specific details of each customized test and the material test results are described in the literature by Crawford et al.<sup>15</sup> The test results provide a comprehensive assessment of the material performance in tension and compression over a broad range of engineering strain rates given.

Material characterization tests include the following:

- Monotonic uniaxial tension tests ( $\cong 0.01 \text{ s}^{-1}$ ,  $0.10 \text{ s}^{-1}$ ,  $1.0 \text{ s}^{-1}$  engineering strain rate)
- Monotonic uniaxial compression tests ( $\cong 0.01 \text{ s}^{-1}$ ,  $0.10 \text{ s}^{-1}$ ,  $1.0 \text{ s}^{-1}$  engineering strain rate)
- The cyclic uniaxial tension tests ( $0.0033 \text{ s}^{-1}$ ,  $0.033 \text{ s}^{-1}$ ,  $0.33 \text{ s}^{-1}$  engineering strain rate)
- The cyclic uniaxial compression tests ( $0.01 \text{ s}^{-1}$ ,  $0.10 \text{ s}^{-1}$ ,  $1.0 \text{ s}^{-1}$  engineering strain rate)
- High rate drop tower – tension ( $30$  and  $400 \text{ s}^{-1}$ )
- High rate drop tower – compression ( $\cong 50$  and  $150 \text{ s}^{-1}$ )
- Split Hopkinson pressure bar (SHPB) – compression ( $\cong 500$  and  $1000 \text{ s}^{-1}$ )
- Bulk modulus, room temperature ( $\cong 0.01 \text{ s}^{-1}$ )
- Failure test ( $\cong 0.01 \text{ s}^{-1}$ ), *where,  $\text{s}^{-1}$  is per second or  $\frac{1}{\text{second}}$*

The Veryst test result summary of mechanical response behavior of the tested materials is presented in Table 1.

**Table 1** Veryst engineering materials tests analyses summary

<b>Material type</b>	<b>Trade name</b>	<b>Location in WIAMan</b>	<b>Dominant material behavior</b>	<b>Recommended material model</b>
Polyurethane	Proflex 30	Pelvis flesh	A nonlinear viscoelastic response with strain-rate effect	Both a simple hyperelastic or a more accurate nonlinear viscoelastic material model
Polyurethane	XE1031	Foot flesh	A nonlinear viscoelastic response with strain-rate effect	A nonlinear viscoelastic
Polyurethane	FD70	Foot plate	A nonlinear viscoelastic response with strain-rate effect	A nonlinear viscoelastic
Acetal resin	Delrin	Calcaneus cap	A nonlinear viscoelastic response with strain-rate effect	A nonlinear viscoelastic
Polyurethane	E1030AL	Flesh-other	A nonlinear viscoelastic response with a little strain-rate effect	A nonlinear viscoelastic
Butyl rubber	75 Shore A (Custom)	Leg and spine compliant elements	A nonlinear viscoelastic response with a strong strain-rate effect	A nonlinear viscoelastic
Polyurethane	Rencast 6425	Tailbone	A nonlinear viscoelastic response with a strong strain-rate effect	A nonlinear viscoelastic
Polyurethane	TC892	Pelvic bone	A nonlinear viscoelastic response with a little strain-rate effect	A nonlinear viscoelastic

Based on the material test data, nonlinear viscoelastic and viscoplastic multirate material models were fit to the experimental data to develop the constitutive material models by both M&S teams. Final selection of the material model approach was determined based on 1) the best fit to the stress-strain curves for each material and 2) stability of the material over the variety of applied loading conditions. Two different approaches to material characterization used by 2 independent M&S teams are described next.

### 3. Velodyne Material Models

The following sections describe the material constitutive models used in the WIAMan Velodyne model, which relate an element's deformation to the resulting internal stress state. The materials models in the Velodyne ATD model are all in agreement with the recommended material models suggested by Veryst Engineering (see Table 1).



### 3.1 Parameterization Procedure

The following 8 polymeric materials in Table 2 were tested and characterized by Veryst Engineering. These materials were selected for testing as there were no available large-strain, high-strain-rate characterization data of the materials chosen for the WIAMan TD. Also, these materials are very compliant relative to the metallic structural components and thus strongly influence the WIAMan ATD response compared to the metals as quantified by the load cells and accelerometers responses due to vertical accelerative loading.

**Table 2** Veryst material tests

Material type	Trade name	Location in WIAMan	Velodyne model
Polyurethane	Proflex 30	Pelvis flesh	proflex30_ogv
Polyurethane	XE1031	Foot flesh	Foot_Flesh_Fit3
Polyurethane	FD70	Foot plate	Foot_Plate_ogv
Acetal resin	Delrin	Calcaneus cap	Calcaneus_Cap_ogv
Polyurethane	E1030AL	Flesh-other	flesh_og_visco
Butyl rubber	75 Shore A (Custom)	Compliant elements	Veryst_BR75A_og_visco
Polyurethane	Rencast 6425	Tailbone	rencast_ogv
Polyurethane	TC892	Pelvic bone	tc892_OGV

For each of the materials shown in Table 2, Veryst performed a variety of material characterization tests at different strain rates. Measured forces and displacements (using digital image correlation for tensile testing and fiducial marker tracking for compression) were extracted from the experimental data and converted into the true stress–true strain plots summarized in Fig. 3. The low-speed compression tests were performed with an MTS rig up to a strain rate of  $1.0 \text{ s}^{-1}$ , and the higher-strain-rate compression tests were performed in a drop rig. Additional detail on the Veryst testing methodology and results can be found in the material characterization reports available through the WIAMan EO.<sup>15</sup>

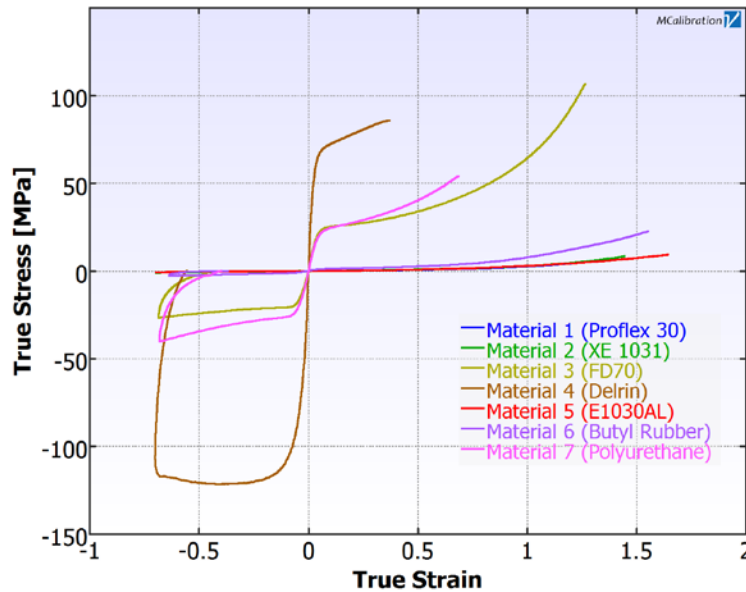


**Fig. 3** Veryst stress-strain results at 0.1/s strain rate

The stress-strain data provided the basis for the Corvid material model fitting procedure. The quasistatic and high-rate compression test data were used exclusively for the fitting procedure with the understanding that most of these materials would be predominately loaded in compression within the WIAMan. Note that this approach then assumes that the tensile response is approximately equivalent to the compressive response. Each of the compressive material test cases was replicated in Velodyne using the actual geometry of the specific test specimen. An example of the Proflex 30 pelvis flesh compression material test specimen as compared to the computational specimen is depicted in Fig. 4. The test specimen in this case was meshed with 4,620 solid hexahedral single integration point elements.

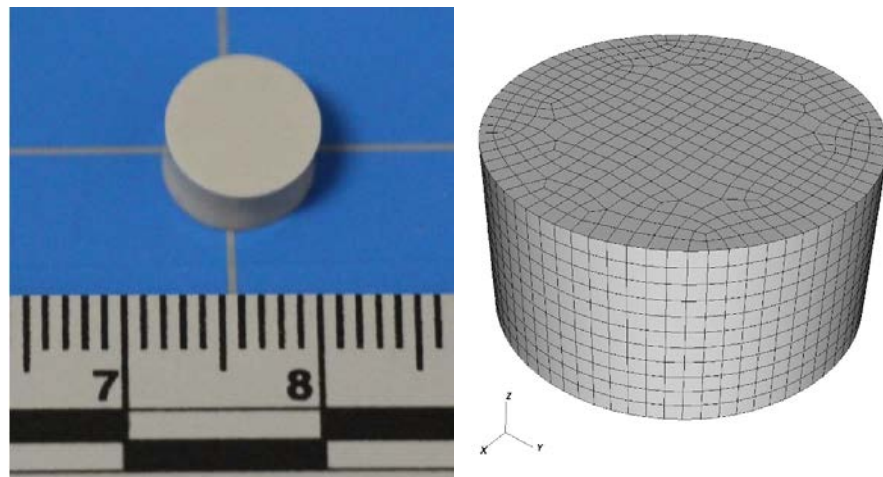


**Fig. 4** The Veryst Proflex 30 compression material test specimen (left) and the FE mesh counterpart (right)

The displacement time history for each compression test (all strain rates) was calculated from the known sample geometry and the true strain output from test, and served as the boundary condition for the FE simulation (while the opposite face of the specimen was fixed from displacing in the direction of the compression). The specimen is free to expand in the lateral x- and y-directions. The boundary conditions applied to the analyses were chosen to replicate the testing conditions as closely as possible. A simple schematic of the computational material compression test is shown in Fig. 5.

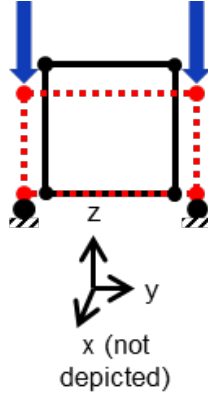


**Fig. 5 Velodyne schematic for the Veryst compression testing**

Based on the polymeric/rubber nature of these materials, the Corvid material fitting procedure employed an additive, nonlinear, hyper-viscoelastic constitutive model, where the stress is the sum of the hyperelastic stress model and the viscoelastic stress model:

$$\sigma = \sigma_{hyper} + \sigma_{visco}. \quad (1)$$

The additive split between hyperelastic and viscoelastic stress contributions provides the ability to solve for the deformation gradient, strain invariants, and strain rate tensor directly. Hyperelastic material models are typically described by strain energy density functions,  $\psi$ , which is often a function of the principal stretches,  $\lambda_i$ , or strain invariants,  $I_i$ . The strain energy density form, Eq. 2, for an Ogden rubber material is written in terms of the principal stretch components. The Ogden model<sup>16</sup> is particularly useful for its relations to other existing models, as it reduces to the Mooney-Rivlin<sup>17</sup> when  $m = 2$  and  $\alpha_{1,2} = 2, -2$  and to the Neo-Hookean model<sup>18</sup> when  $m = 1$  and  $\alpha_1 = 2$ . This aspect gives it a broad range of applicability.

$$\psi_{Ogden} = \sum_{m=1}^n \left\{ \frac{\mu_m}{\alpha_m} \left[ J^{-\alpha_m/3} (\lambda_1^{\alpha_m} + \lambda_2^{\alpha_m} + \lambda_3^{\alpha_m} - 3) \right] \right\} + \frac{K}{2} (J - 1)^2. \quad (2)$$

In Eq. 2,  $\mu_m$  and  $\alpha_m$  are the Ogden fitting parameters that can take on any real values, while the material parameter  $K$  is a measure of the shear moduli, which must be a positive nonzero real value.

The hyperelastic portion of the stress is calculated using the Ogden nonlinear elastic model as shown:

$$\boldsymbol{\sigma}_{hyper} = \frac{1}{J} \mathbf{F} \left\{ \frac{\partial \psi_{ogden}}{\partial \mathbf{E}} (\mathbf{E}(\tau)) \right\} \mathbf{F}^T. \quad (3)$$

The viscoelastic model by Li and Lau<sup>19</sup> is as shown:

$$\boldsymbol{\sigma}_{visco} = \frac{1}{J} \mathbf{F} \left\{ \int_0^t [A_1 + A_2(I_2 - 3)] \left[ \sum_{i=1}^6 G_i e^{-(t-\tau)/T_i} \right] \dot{\mathbf{E}}(\tau) d\tau \right\} \mathbf{F}^T. \quad (4)$$

The convolution integral was solved either through direct numerical integration or a state variables approach. Both methods were evaluated, but the state variable approach, which has better numerical efficiency with similar numerical error to that of the direct integration method, was used to produce all subsequent results. In Eq. 4, the viscoelastic model parameters  $G_i$  and  $T_i$  are the shear relaxation moduli and relaxation times, which make up the classical Prony series. A Prony-series expansion is a relaxation function approximation for modeling time-dependent damping. The scalar parameters  $A_1$  and  $A_2$  control the nonlinearity of the Prony series. Under the conditions  $A_1 = 1$  and  $A_2 = 0$ , the model reduces to the standard Prony series viscoelastic model.

A 2-step (systematic calibration) material model parameter optimization procedure was employed for all materials. A systematic optimization was chosen given the quasistatic data and the additive nature of the material model in predicting stress (Eq. 1). The additive decomposition of the stress into hyperelastic and viscoelastic stresses allows for one to distinguish the viscoelastic effects from the hyperelastic effects by calibrating the material responses to the quasistatic data where strain rates become insensitive. For the hyperelastic parameters (Eq. 2), an optimization routine is performed for the material characterization test simulations at the lowest available compressive strain rate to establish the quasistatic behavior. These parameters were then locked for the rest of the process. Once the hyperelastic parameters are determined, a second optimization procedure is used to solve for the Prony series parameters (Eq. 4) that control the viscous dissipation. In this second step, all higher-rate tests are simulated to cover the full range of material rate effects over all available strain rates. These fits are then tested to verify the material parameter set, in addition to large deformation stability test simulations. If instabilities are indicated, then a lower order fit may be used as is the case with the

TC892 pelvic bone to preserve stability. This process was repeated for all the materials presented here, and the results are discussed in the following.

Inverse analysis using nonlinear least-squares regression methods were applied to determine the material model parameters within Velodyne that best fit the experimental stress-strain data. To do so, the Design Analysis Kit for Optimization and Terascale Applications (DAKOTA),<sup>20</sup> a software package maintained by Sandia National Laboratories, was used to integrate Velodyne input and output with parallelization and optimization tools provided within DAKOTA and automate the linear regression process. Available worldwide under a GNU Lesser General Public License at no cost, DAKOTA offers several advantages over other optimization and integration software in that it provides parallel analysis and optimization tools that other facilities do not. Given the similar parallel capabilities of Velodyne, DAKOTA is a natural choice as an automated parallel iterator and decision maker when implemented on a high-performance cluster.

The process flow for inverse analysis of parameter determination of a material model is shown in Fig. 6. After initialization, DAKOTA passes input to a Python script that updates material parameters for Velodyne. DAKOTA then spawns a number of Velodyne analyses on sets of separate processors, each of which can take advantage of parallel processing capabilities by using the individually allocated processors. Currently, these processors are allocated at the time an individual process is spawned, allowing reallocation of computational resource as needed. Upon completion, user-defined responses are calculated via a Python script. Then a stopping criterion (e.g., convergence value or maximum iteration number) is checked. If the check succeeds, output is written to files for postprocessing. If the check fails, a decision is made to update parameters via an optimization method through DAKOTA and the process iterates.

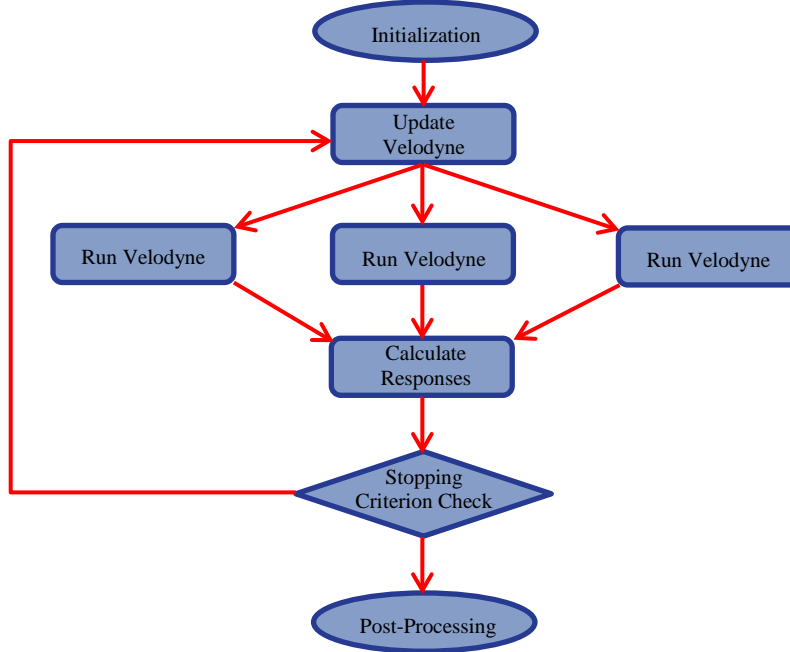


**Fig. 6 Process flow for inverse analysis using DAKOTA to iterate parallel runs of Velodyne**

A standard response or objective function used for inverse analysis is the nonlinear least-squares response. For a data set containing stress versus strain data, the response  $f$  is calculated as

$$f = \sum_{i=1}^n (\sigma_i^A(\mathbf{p}) - \sigma_i^E)^2, \quad (5)$$

where  $\sigma_i^A(\mathbf{p})$ , a function of parameters  $\mathbf{p}$ , is the engineering stress at point  $i$  in strain found from the analysis and  $\sigma_i^E$  is the experimental value of the stress at strain  $i$ . An ideal response, representing a perfect fit of the experimental data with the material model, has a value  $f = 0$ . For fitting multiple strain rates, the objective function becomes a sum of all the fitness values for each strain rate where the least-squares response,  $R$ , was determined according to

$$R = \sum_{k=1}^N \sum_{m=1}^n \left( \frac{(\sigma_m^A(\mathbf{p}) - \sigma_m^E)^2}{n} \right)^{1/2}, \quad (6)$$

where  $N$  is the number of stress-strain histories used for calibration,  $n$  is the number of individual points a provided stress-strain history for curve  $k$ ,  $\sigma_m^A$  is the Cauchy stress at engineering strain  $E_m^E$  given by the model with parameters  $\mathbf{p}$ , and  $\sigma_m^E$  is the experimental Cauchy stress at the same strain.

The optimization problem is a nonlinear least-squares inverse analysis searching for a minimum to a multimodal objective function of Eq. 6 subject to various inequality constraints given by

$$\begin{aligned}
& \min R(\mathbf{p}) \\
& \text{subject to: } G^{lb} \leq G^{el} \leq G^{ub} \\
& \quad v^{lb} \leq v \leq v^{ub} \quad ,
\end{aligned} \tag{7}$$

where  $G^{el}$ , is the initial tangent elastic shear moduli that should be bounded between a lower and upper bound based on material literature and the initial tangent modulus of the uniaxial stress-strain compression responses. Another nonlinear constraint to consider in the optimization of both rubbers and foams is that the Poisson ratio,  $v$  should be bounded by lower and upper limits. For rubber materials, the Poisson ratio should be high enough for nearly incompressible behavior, which practical bounds were found to be between  $0.450 \leq v \leq 0.499$ . The Poisson ratio of a material can be calculated based on the bulk and shear modulus

$$v = \frac{3K-2G}{6K+2G} \quad , \tag{8}$$

such that for nearly incompressible material behavior, the bulk modulus should be significantly larger than the shear modulus,  $K \gg G$ . Also, for rubber materials, incompressibility has been found to be essential in accurately predicting the viscoelastic behavior. In contrast, foam materials are much more compressible and the Poisson ratio has been found to be suitable between  $0 \leq v \leq 0.3$ .

To update the parameters and control the process, an optimization algorithm was used as the decision maker. Each material model has a different level of complication in terms of number of parameters and sensitivity to change in parameters, making necessary the use of an algorithm that accounts for these issues while also considering computational and wall clock time costs. Historically, deterministic methods (e.g., methods that use derivatives to mathematically check for convergence) are largely computationally efficient, but they suffer from convergence issues, being easily trapped in local minima rather than finding a globally minimum response value. To alleviate some of these issues, heuristics methods are married with the deterministic algorithms, increasing the likelihood of obtaining a global minimum. On the other hand, nondeterministic methods (e.g., genetic and evolutionary algorithms) require large numbers of iterations, making them computationally much more expensive. However, they are often much more robust when combined with heuristics, often being able to find one or a number of global minima if they exist.

In this study, the single objective genetic algorithm (SOGA) available in DAKOTA was used as the primary optimization algorithm for running the FE analysis of the actual samples in Velodyne. For the genetic algorithm, a population size of 100 points with 200 maximum number of generations specified giving a maximum of 20,000 function evaluations. In addition, the deterministic quasi-Newton method available from the OPT++ package (optpp\_q\_newton) available in DAKOTA was explored in

conjunction with a multistart heuristic algorithm. The multistart algorithm chooses a specified number of starting points, 8 in this case, from the design space randomly, running separate optimizations from each point. For a single point, a maximum number of 100 iterations was specified. However, the deterministic algorithms in DAKOTA seem to be prone to premature convergence, thus the stochastic method of a genetic algorithm was leveraged more for optimization use in DAKOTA.

### **3.2 Results for Velodyne Materials Models**

---

Using the approach outlined previously, the optimized material characterization parameters are presented for each material characterized by Veryst testing. The material parameters presented in this report have been validated well against subsystem and whole-body tests, and they were stable enough to run at durability and higher levels (Corvid validation document<sup>8</sup>). A few iterations of material fits (not reported in the report) were required for some materials, for example, for the foot flesh, to overcome the instability issues in running durability and higher levels of loading simulations of the components or whole-body ATD tests. Additionally, a comparison of the model performance relative to experimental data is presented.

Hyperelastic and viscoelastic Velodyne material model parameters and corresponding comparison of Ogden viscoelastic model response to experimental data for 8 polymeric materials are shown in Tables 3–18 and Figs. 7–14, respectively. In general, the Ogden material model for the softer materials (pelvis flesh [Fig. 7], foot flesh [Fig. 8], and other flesh [Fig. 11]) fit well with experimental data for various strain rates. As for the harder plastics (foot plate [Fig. 9], butyl rubber [Fig. 12], tailbone [Fig. 13], and pelvis bone [Fig. 14]), the Ogden model did not predict responses at the higher strain rates as closely. It should be noted that for the harder plastic models, the higher-strain-rate predictions deviated from the respective experimental responses at larger strains due to complexity of the concurrent effects of viscoelastic and viscoplastic responses. A different material model, as is shown in the LS-DYNA case, could reduce the gaps between the simulation and experimental response at large strains, but at the cost of accounting for the viscoelastic effects at more WIAMan application relevant strains. Further refinement of the material model parameter estimation (for the Velodyne analyses) was not conducted to match the experimental response into the plastic strain regime of the test coupons mainly because the material models presented here produced excellent results within the elastic regime and acceptable results in the plastic regime. This assertion is supported by the successful validation of the WIAMan Velodyne model with in whole-body simulations<sup>6</sup>, confirming that the ATD FEM model was capable of predictive models and ready to support the demanding nature of the applications need and meet the ATD design development milestone.



### 3.2.1 Proflex 30 Pelvis Flesh

**Table 3 Hyperelastic fit parameters for the Proflex 30 pelvis flesh**

$\rho$ (kg/m <sup>3</sup> )	$\mu_1$ [MPa]	$\mu_2$ [MPa]	$\mu_3$ [MPa]	$\alpha_1$	$\alpha_2$	$\alpha_3$	K [MPa]
1040	-0.183	0.801	0.698	-1.425	-0.593	1.640	21.67

**Table 4 Viscous fit parameters for the Proflex 30 pelvis flesh**

$G_1$ (MPa)	$G_2$ (MPa)	$G_3$ (MPa)	$G_4$ (MPa)	$G_5$ (MPa)	$G_6$ (MPa)
0.253	0.186	0.551	2.231	2.921	1.204
$T_1$ (s)	$T_2$ (s)	$T_3$ (s)	$T_4$ (s)	$T_5$ (s)	$T_6$ (s)
95.687	7.576E-2	1.08E-4	5.40E-5	3.70E-5	5.82E-8
$A_1$	$A_2$				
0.0713	0.0127				

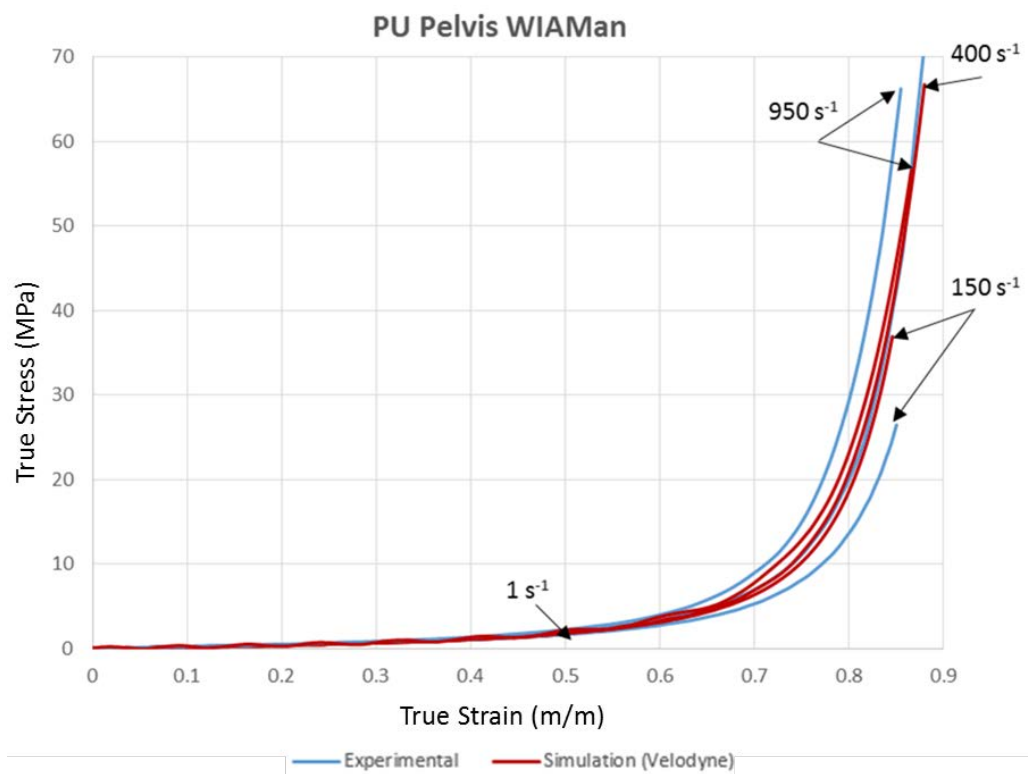


**Fig. 7 Comparison of the Ogden viscoelastic model to experimental compression data for the Proflex 30 pelvis flesh**

### 3.2.2 XE1031 Foot Flesh

**Table 5** Hyperelastic fit parameters for the XE1031 foot flesh

$\rho$ (kg/m <sup>3</sup> )	$\mu_1$ [MPa]	$\mu_2$ [MPa]	$\mu_3$ [MPa]	$\alpha_1$	$\alpha_2$	$\alpha_3$	K [MPa]
1060	0.414	-0.898	-0.974	0.295	-0.686	-0.964	20.0

**Table 6** Viscous fit parameters for the XE1031 foot flesh

$G_1$ (MPa)	$G_2$ (MPa)	$G_3$ (MPa)	$G_4$ (MPa)	$G_5$ (MPa)	$G_6$ (MPa)
0.459	0.011	0.310	2.76	4.04	4.13
$T_1$ (s)	$T_2$ (s)	$T_3$ (s)	$T_4$ (s)	$T_5$ (s)	$T_6$ (s)
7.98	2.86E-2	9.11E-4	5.93E-4	9.10E-5	7.26E-7
$A_1$	$A_2$				
0.011	0.000				

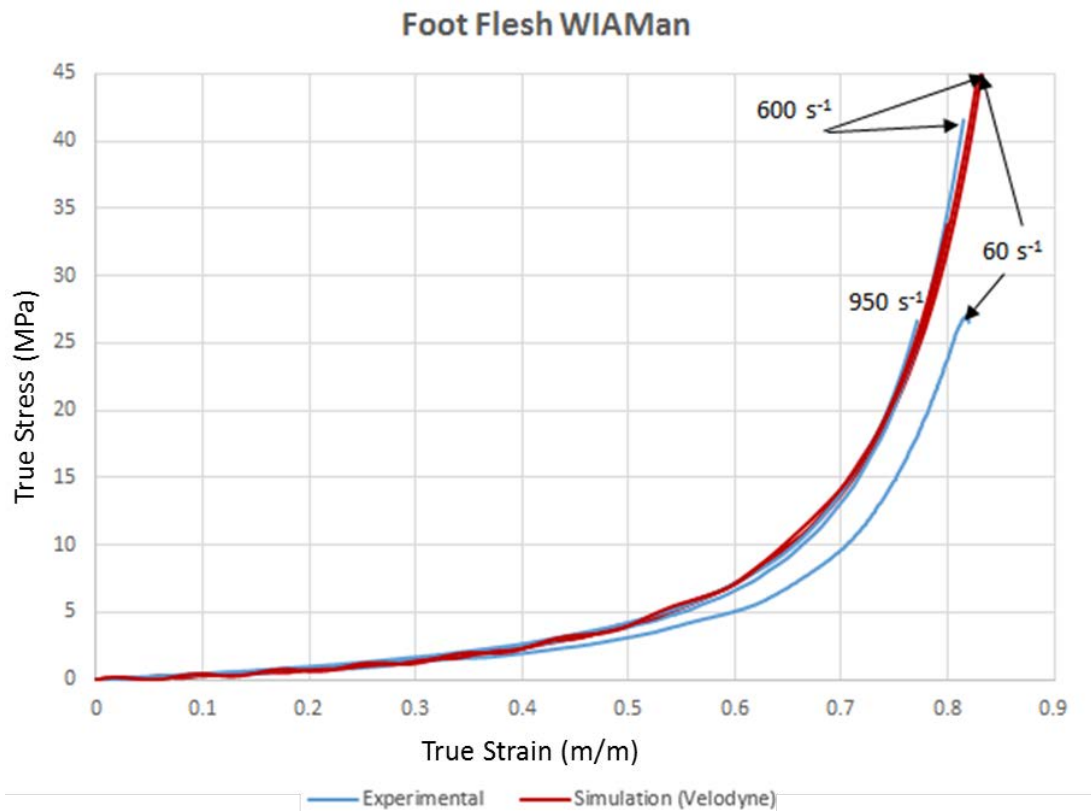


**Fig. 8** Comparison of the Ogden viscoelastic model to experimental compression data for the XE1031 foot flesh

### 3.2.3 FD70 Foot Plate

Table 7 Hyperelastic fit parameters for the FD70 foot plate

$\rho$ (kg/m <sup>3</sup> )	$\mu_1$ [MPa]	$\mu_2$ [MPa]	$\mu_3$ [MPa]	$\mu_4$ [MPa]	$\mu_5$ [MPa]	$\alpha_1$	$\alpha_2$	$\alpha_3$	$\alpha_4$	$\alpha_5$	K [MPa]
1211	-14.595	37.595	-10.613	0.256	43.532	0.637	-5.883	1.632	-2.285	11.362	2500

Table 8 Viscous fit parameters for the FD70 foot plate

$G_1$ (MPa)	$G_2$ (MPa)	$G_3$ (MPa)	$G_4$ (MPa)	$G_5$ (MPa)	$G_6$ (MPa)
42.45	66.66	98.72	95.89	30.096	99.96
$T_1$ (s)	$T_2$ (s)	$T_3$ (s)	$T_4$ (s)	$T_5$ (s)	$T_6$ (s)
35.442	2.48E-2	1.747E-3	5.28E-4	9.64E-5	2.08E-7
$A_1$	$A_2$				
1.000	0.192				

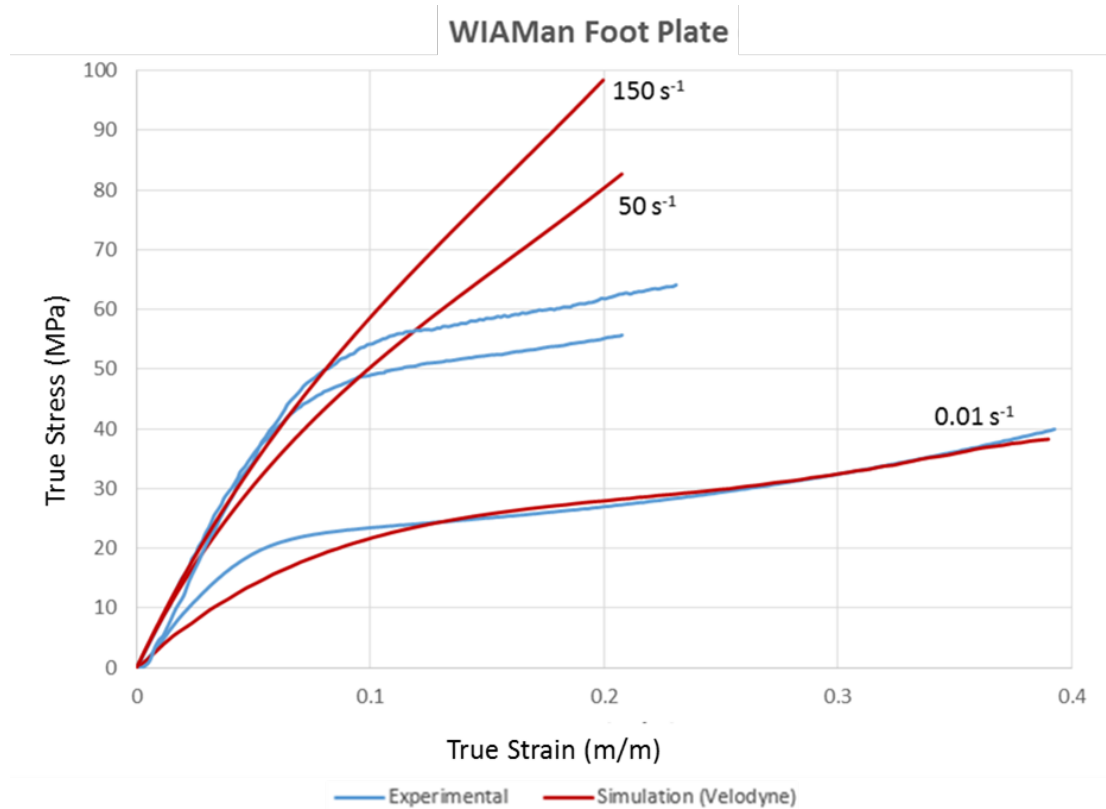


Fig. 9 Comparison of the Ogden viscoelastic model to experimental compression data for the FD70 foot plate

### 3.2.4 Delrin Calcaneus Cap

**Table 9 Hyperelastic fit parameters for the Delrin calcaneus cap**

$\rho$ (kg/m <sup>3</sup> )	$\mu_1$ [MPa]	$\mu_2$ [MPa]	$\mu_3$ [MPa]	$\alpha_1$	$\alpha_2$	$\alpha_3$	$K$ [MPa]	$G_0$ [MPa]*
1410	363.0	762.0	121.0	8.72	-4.15	15.6	2310	942

**Table 10 Viscous fit parameters for the Delrin calcaneus cap**

$G_1$ (MPa)	$G_2$ (MPa)	$G_3$ (MPa)	$G_4$ (MPa)	$G_5$ (MPa)	$G_6$ (MPa)
0.0719	80.3	18.4	83.9	3.29	93.4
$T_1$ (s)	$T_2$ (s)	$T_3$ (s)	$T_4$ (s)	$T_5$ (s)	$T_6$ (s)
12.6	0.686	8.34E-03	7.97E-04	2.33E-05	5.10E-08
$A_1$	$A_2$				
1	0.107				

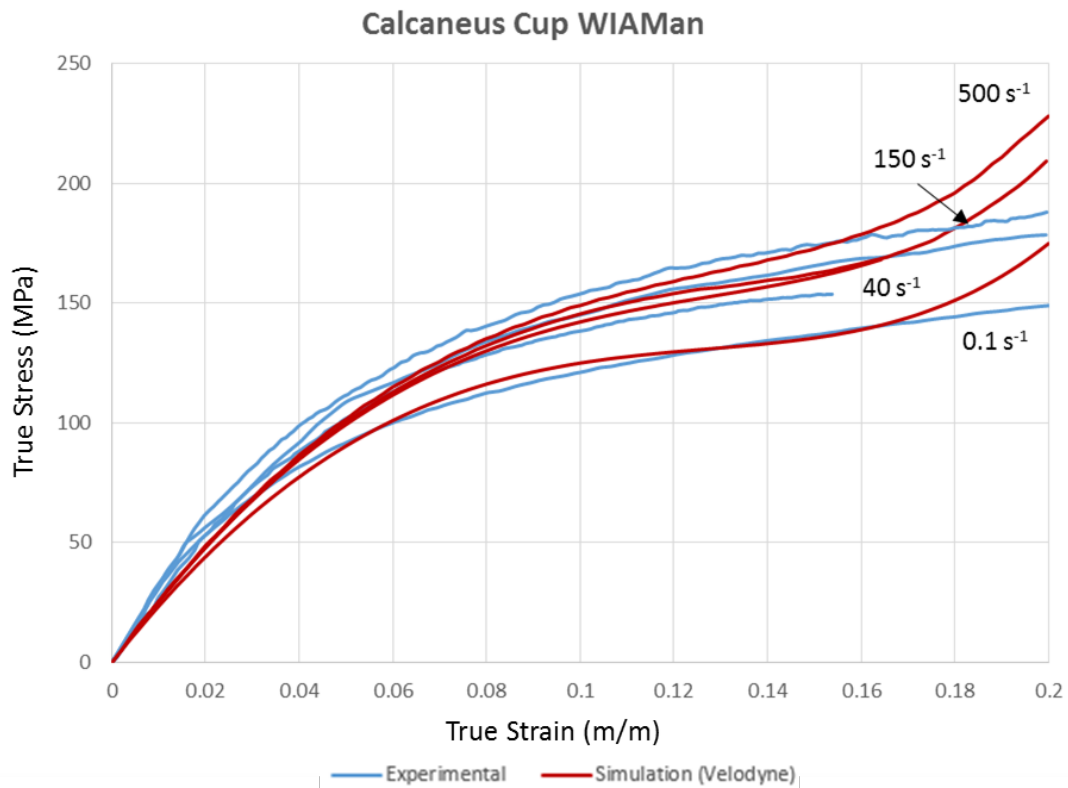


**Fig. 10 Comparison of the Ogden viscoelastic model to experimental compression data for the Delrin calcaneus cap**

### 3.2.5 E1030AL Flesh (Other)

**Table 11 Hyperelastic fit parameters for the E1030AL flesh**

$\rho$ (kg/m <sup>3</sup> )	$\mu_1$ [MPa]	$\mu_2$ [MPa]	$\mu_3$ [MPa]	$\alpha_1$	$\alpha_2$	$\alpha_3$	K [MPa]
1050	-0.227	-0.2478	0.6977	-1.426	-0.4571	0.271	22.07

**Table 12 Viscous fit parameters for the E1030AL flesh**

$G_1$ (MPa)	$G_2$ (MPa)	$G_3$ (MPa)	$G_4$ (MPa)	$G_5$ (MPa)	$G_6$ (MPa)
0.4313	0.879	0.0341	4.625	2.327	1.070
$T_1$ (s)	$T_2$ (s)	$T_3$ (s)	$T_4$ (s)	$T_5$ (s)	$T_6$ (s)
2.202	2.371E-3	2.215E-3	4.20E-4	8.28E-5	8.22E-7
$A_1$	$A_2$				
0.220	0.000				

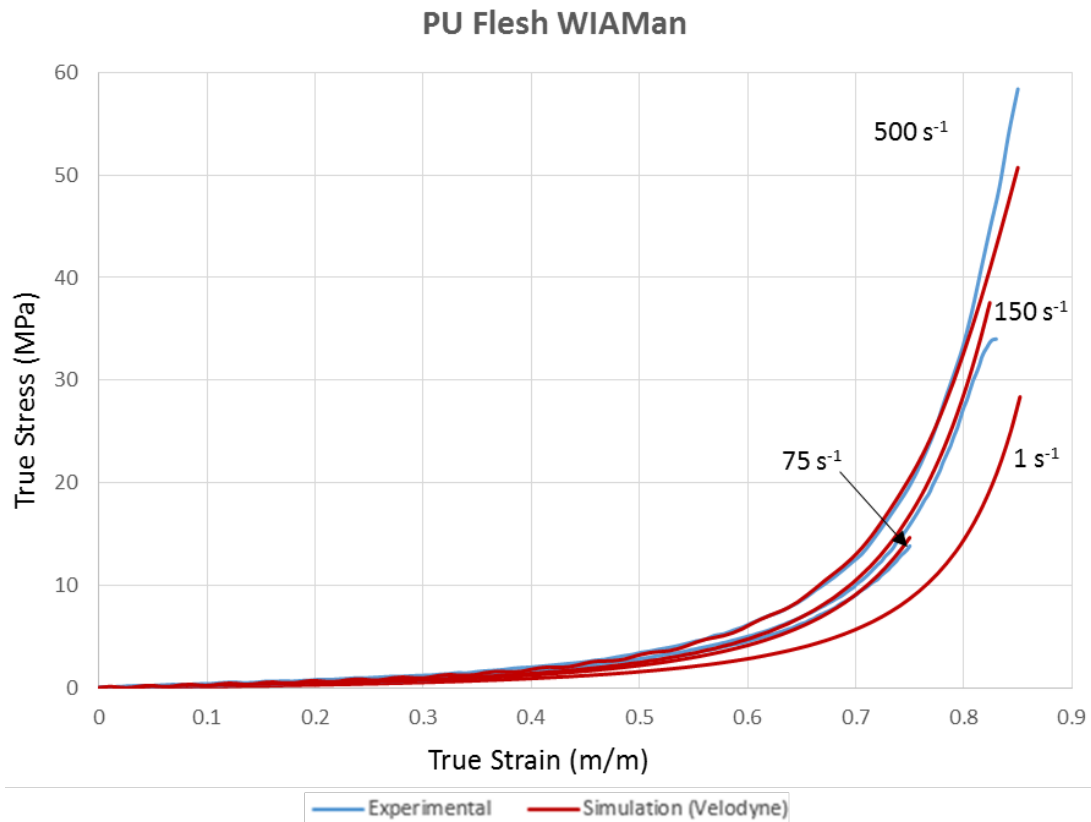


**Fig. 11 Comparison of the Ogden viscoelastic model to experimental compression data for the E1030AL flesh**

### 3.2.6 Butyl Rubber (75 Shore A) Compliant Elements

**Table 13** Hyperelastic fit parameters for the butyl rubber 75A

$\rho$ (kg/m <sup>3</sup> )	$\mu_1$ [MPa]	$\mu_2$ [MPa]	$\mu_3$ [MPa]	$\alpha_1$	$\alpha_2$	$\alpha_3$	K [MPa]
1460	6.042	2.668	-3.854	5.845	-2.935	4.990	150

**Table 14** Viscous fit parameters for the butyl rubber 75A

$G_1$ (MPa)	$G_2$ (MPa)	$G_3$ (MPa)	$G_4$ (MPa)	$G_5$ (MPa)	$G_6$ (MPa)
1.952	11.238	41.270	47.886	24.999	49.863
$T_1$ (s)	$T_2$ (s)	$T_3$ (s)	$T_4$ (s)	$T_5$ (s)	$T_6$ (s)
22.257	6.74E-2	5.314E-3	5.81E-4	8.70E-5	4.60E-7
$A_1$	$A_2$				
1.000	0				

#### Compliant Elements WIAMan

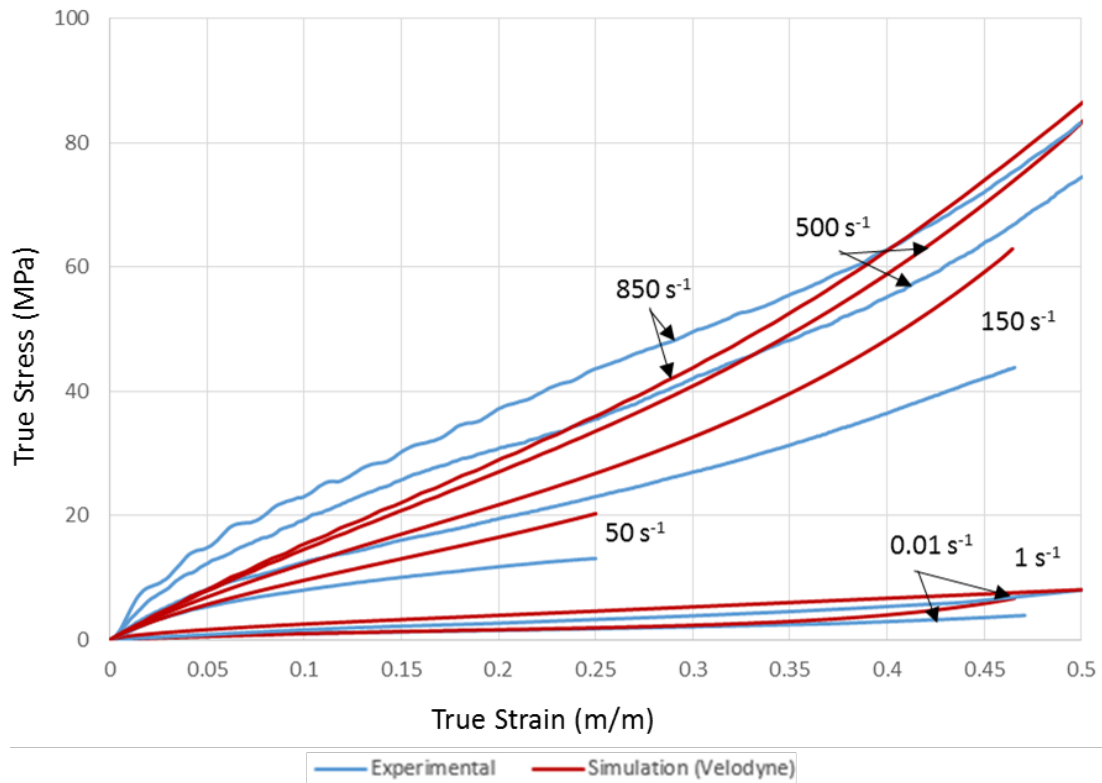


**Fig. 12** Comparison of the Ogden viscoelastic model to experimental compression data for the butyl rubber 75A

### 3.2.7 Rencast 6425 Tailbone

**Table 15 Hyperelastic fit parameters for the Rencast 6425 tailbone**

$\rho$ (kg/m <sup>3</sup> )	$\mu_1$ [MPa]	$\mu_2$ [MPa]	$\mu_3$ [MPa]	$\alpha_1$	$\alpha_2$	$\alpha_3$	$K$ [MPa]
1180	46.50	-25.76	52.20	16.98	-0.128	-7.864	1500

**Table 16 Viscous fit parameters for the Rencast 6425 tailbone**

$G_1$ (MPa)	$G_2$ (MPa)	$G_3$ (MPa)	$G_4$ (MPa)	$G_5$ (MPa)	$G_6$ (MPa)
54.65	42.48	73.12	46.88	95.13	83.94
$T_1$ (s)	$T_2$ (s)	$T_3$ (s)	$T_4$ (s)	$T_5$ (s)	$T_6$ (s)
5.577	0.6393	7.212E-2	3.955E-4	8.537E-5	1.699E-7
$A_1$	$A_2$				
1	0.0636				

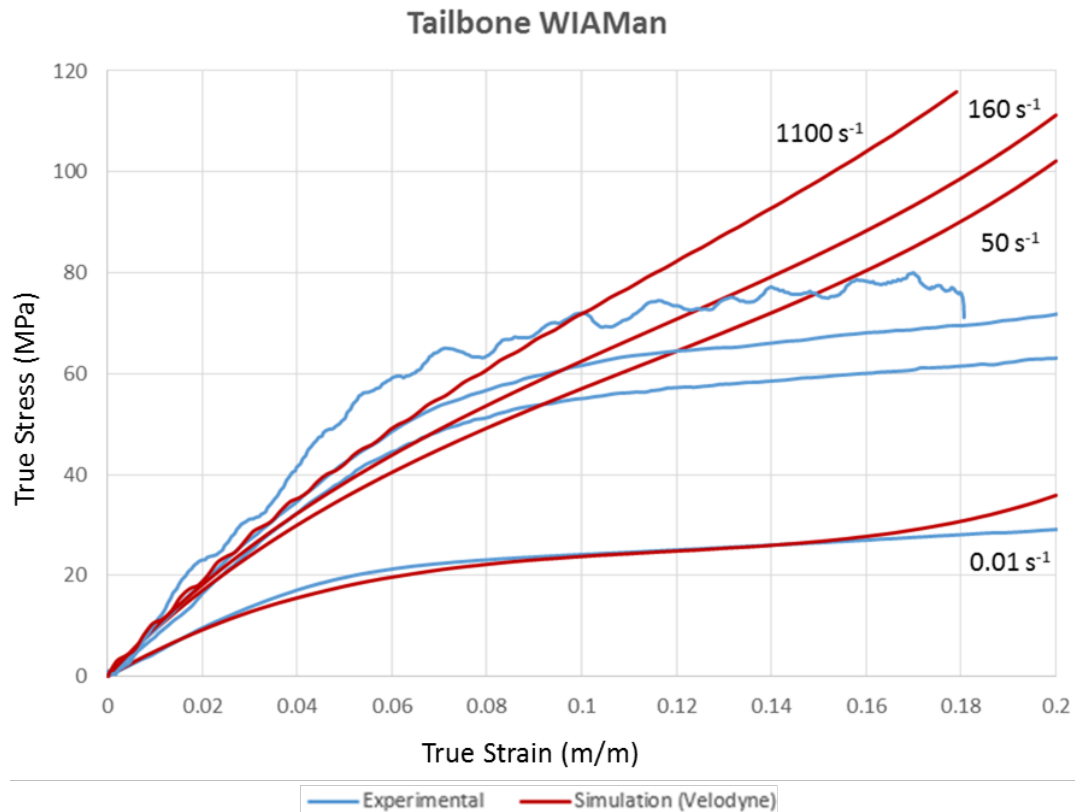


**Fig. 13 Comparison of the Ogden viscoelastic model to experimental compression data for the Rencast 6425 tailbone**

### 3.2.8 TC892 Pelvis Bone

**Table 17** Hyperelastic fit parameters for the TC892 pelvis bone

$\rho$ (kg/m <sup>3</sup> )	$\mu_1$ [MPa]	$\mu_2$ [MPa]	$\mu_3$ [MPa]	$\alpha_1$	$\alpha_2$	$\alpha_3$	<b>K</b> [MPa]
1160	665	-	-	2	-	-	10000

**Table 18** Viscous fit parameters for the TC892 pelvis bone

$G_1$ (MPa)	$G_2$ (MPa)	$G_3$ (MPa)	$G_4$ (MPa)	$G_5$ (MPa)	$G_6$ (MPa)
1.819	0.843	1.485	26.4	36.893	47.234
$T_1$ (s)	$T_2$ (s)	$T_3$ (s)	$T_4$ (s)	$T_5$ (s)	$T_6$ (s)
35.016	0.143	5.315E-2	3.33E-4	2.14E-5	6.61E-7
$A_1$	$A_2$				
1.000	0.000				

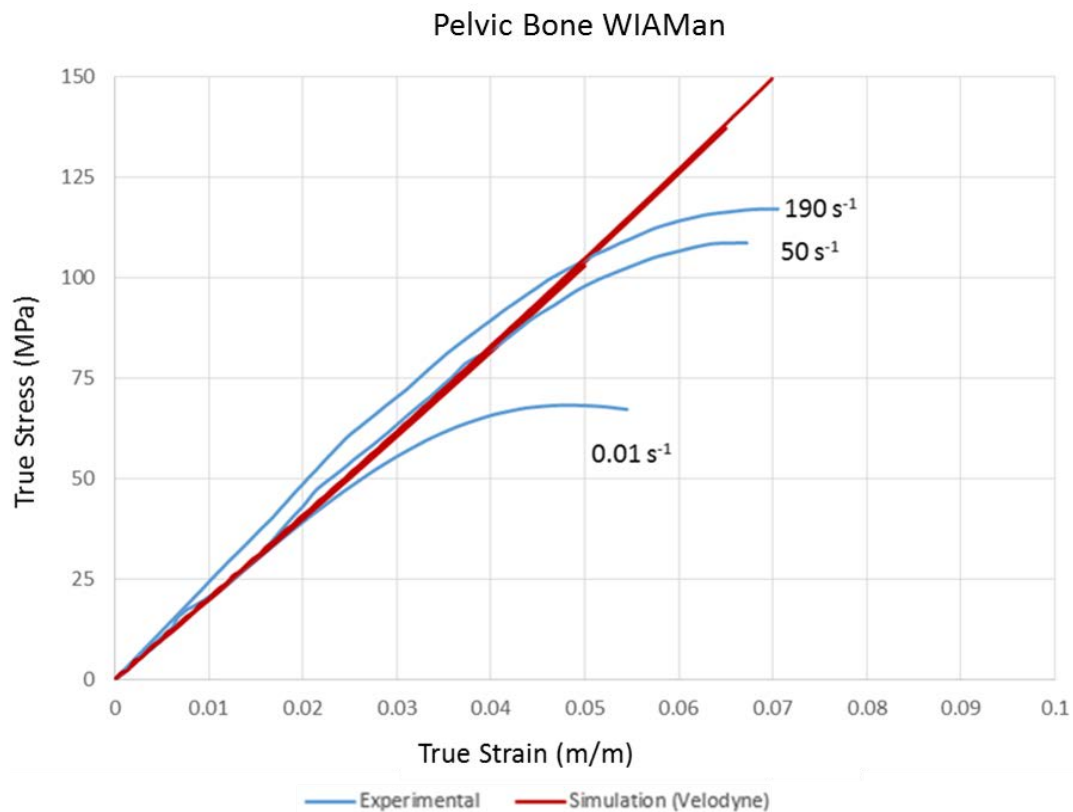


**Fig. 14** Comparison of the Ogden viscoelastic model to experimental compression data for the TC892 pelvis bone



## 4. LS-DYNA Material Models

The LS-DYNA material characterization was performed with multirate compression and tension testing on most of the plastic and rubber materials used in the dummy. Material models were created based on all of the available characterizations. Typically, an Ogden or Bergstrom-Boyce (BB) material model was used for soft materials such as the flesh. The material models were subsequently validated in the subassembly level validation.

Table 19 features the polymer materials used in the LS-DYNA WIAMan model and lists where these materials are used; what material model is used to represent them; the strain rate range used to fit the material models; and the material library identification number.

**Table 19 WIAMan LS-DYNA polymer materials**

Material name	Anatomic location(s)	LS-DYNA material model	Strain rate range fitted	Material library ID
Butyl rubber 75 Shore A	Compliant elements; spine rubber	*MAT_OGDEN_RUBBER	T: - C: 1-850	58
Proflex 30	Pelvis flesh	*MAT_BERGSTROM_BOYCE_RUBBER	T: 0.003-300 C: 0.01-950	59
E1030AL	Flesh-other	*MAT_BERGSTROM_BOYCE_RUBBER	T: 1-90 C: 1-850	60
XE1031	Foot flesh	*MAT_OGDEN_RUBBER	T: - C: 1-600	61
FD70	Foot plate	*MAT_SIMPLIFIED_JOHNSON_COOK	T: 1-75 C: 1-150	62
Delrin	Calcaneus cap	*MAT_SIMPLIFIED_JOHNSON_COOK	T: 1-50 C: 40-600	63
TC892	Pelvic bone	*MAT_SIMPLIFIED_JOHNSON_COOK	T: 1-80 C: 1-550	64
Rencast 6425	Tailbone	*MAT_SIMPLIFIED_JOHNSON_COOK	T: 1-300 C: 1-160	65
ISODAMP	Heel plug	*MAT_OGDEN_RUBBER	T: 1-300 C: 1-160	68

Note: T is tension and C is compression.

There are also several polymer materials used in the WIAMan that either require less fidelity than those listed previously or no test data were available for a material fit procedure to be performed. These materials were assigned Blatz-Ko Rubber material parameters based upon the durometer specified for the given materials. With the exception of the rubber representing the boot treads (inherited from the US Army Research Laboratory [ARL] in the boot model) and the molded neck rubber (optimized based upon experimental tests), the durometers were converted to elastic moduli (followed by a conversion to shear moduli) according to Qi et al.<sup>21</sup> in Eq. 9):

$$E = 0.0235S - 0.6403$$

$$S = \begin{cases} \text{Shore A } 20A < S < 80A \\ \text{Shore D } + 50 \text{ } 80A < S < 85D \end{cases}$$

$$G = \frac{E}{2(1+\nu)} . \quad (9)$$

## 4.1 Polymer Material Models

---

Four different LS-DYNA polymeric material models (Bergstrom\_Boyce, Ogden\_Rubber, Simplified\_Johnson\_Cook, and Blatz\_KO\_Rubber) have been used in the LS-DYNA FE modeling of the WIAMan ATD. Final selection of the material models in the WIAMan FEM was based on the stability of the material model behavior over a variety of applied loading conditions. For example, BERGSTROM\_BOYCE model showed poor correlation among the experimental and simulation results when compared in the cervical spine (compliant material) component model case. However, a change in the material model from BERGSTROM\_BOYCE to the Ogden material model resulted in a much better correlation of simulation results as discussed in the polymer fitting procedure in Section 4.2. A brief outline of constitutive equations describing the fundamental behavior of the models are described next.

### 4.1.1 \*MAT\_OGDEN\_RUBBER

Hyperelastic materials are a class of elastic materials for which the stress-strain relationship is dependent upon a strain energy potential function; materials of this type can reach beyond standard linear elasticity in that the strain energy function provides for work-path independence and options for nonlinear elasticity and near-incompressibility. Rubber materials often exhibit hyperelastic qualities and therefore are often idealized as incompressible hyperelastic materials. The standard Ogden model is a well-known and commonly used hyperelastic constitutive model. Alone, the Ogden model cannot exhibit rate-dependent properties, but the addition of a viscoelastic material model superimposed upon the Ogden model allows for rate sensitivity. The LS-DYNA implementation<sup>22</sup> has the option to add viscoelasticity to the Ogden model with a Prony series (a Maxwell fluid-type model consisting of springs and dampers in series) shown in the following equations.

$$\text{Hyperelastic Ogden Model: } \begin{cases} W(\lambda_1, \lambda_2, \lambda_3) = \sum_{p=1}^N \frac{\mu_p}{\alpha_p} (\lambda_1^{\alpha_p} + \lambda_2^{\alpha_p} + \lambda_3^{\alpha_p} - 3) \\ \sigma_j = p + \lambda_j \frac{\partial W}{\partial \lambda_j} \end{cases} , \quad (10)$$

with  $W$  as the strain energy potential as a function of the principal stretches  $\lambda_i$ ;  $p$  as the pressure;  $\mu_p$ ,  $\alpha_p$ , and  $N$  as material constants; and  $\sigma_j$  as the principal Cauchy stresses.

$$\text{Viscoelastic Prony Series: } \begin{cases} \sigma_{ij} = \int_0^t g_{ijkl}(t - \tau) \frac{\partial \varepsilon_{kl}}{\partial \tau} d\tau, \\ g(t) = \sum_{i=1}^n G_i e^{-\beta_i t} \end{cases}, \quad (11)$$

with  $\sigma_{ij}$  as the Cauchy stresses,  $t$  as time,  $G_i$  as shear moduli, and  $\beta_i$  as decay constants.

#### 4.1.2 \*MAT\_BERGSTROM\_BOYCE\_RUBBER

The BB material model is a viscoplastic model, consisting of Arruda-Boyce 8-chain hyperelastic models and a viscous flow model. The Arruda-Boyce model is a hyperelastic polymer model based upon statistical mechanics and the finite extensibility of a polymer chain.<sup>23</sup> Its rheological representation is that of parallel paths A and B, each containing an Arruda-Boyce hyperelastic “spring”, but with a viscous damper placed in series with the spring in Path B. The deviatoric Kirchhoff stress is computed as shown in the following equations:

$$\begin{aligned} \bar{\boldsymbol{\tau}} &= \boldsymbol{\tau}_A + \boldsymbol{\tau}_B \\ \text{Elastic Path A} &\left\{ \begin{aligned} \boldsymbol{\tau}_A &= \frac{G}{3} \frac{3 - \lambda_r^2}{1 - \lambda_r^2} \left( \bar{\mathbf{b}} - \frac{\text{Tr}(\bar{\mathbf{b}})}{3} \mathbf{I} \right) \\ G &\text{ is the elastic shear modulus,} \\ \bar{\mathbf{b}} &= J^{-2/3} \mathbf{F} \mathbf{F}^T \\ J &= \det(\mathbf{F}) \\ &\text{is the unimodular left Cauchy Green tensor, and} \\ \lambda_r^2 &= \frac{\text{Tr}(\bar{\mathbf{b}})}{3N} \\ &\text{is the relative network stretch} \end{aligned} \right. \quad (12) \end{aligned}$$

Viscoelastic Path B {

Perform a multiplicative split of the deformation gradient into elastic and inelastic parts

$$J^{1/3} \mathbf{F} = \mathbf{F}_e \mathbf{F}_i$$

$$\mathbf{b}_e = \mathbf{F}_e \mathbf{F}_e^T$$

$$\boldsymbol{\tau}_B = \frac{G_v}{3} \frac{3 - \lambda_v^2}{1 - \lambda_v^2} \left( \mathbf{b}_e - \frac{\text{Tr}(\mathbf{b}_e)}{3} \mathbf{I} \right)$$

This time  $G_v$  is the shear modulus for Path B, the relative network stretch is

$$\lambda_v^2 = \frac{\text{Tr}(\mathbf{b}_e)}{3N_v}$$

the left Cauchy Green Tensor is evolved via

$$\dot{\mathbf{b}}_e = \bar{\mathbf{L}} \mathbf{b}_e + \mathbf{b}_e \bar{\mathbf{L}}^T - 2\mathbf{D}_i \mathbf{b}_e$$

the inelastic rate of deformation tensor is

$$\mathbf{D}_i = \dot{\gamma}_0 (\lambda_i - 0.999)^c \left( \frac{\|\boldsymbol{\tau}_B\|}{\bar{\tau}\sqrt{2}} \right)^m \frac{\boldsymbol{\tau}_B}{\|\boldsymbol{\tau}_B\|}$$

$$\lambda_i^2 = \frac{\text{Tr}(\mathbf{F}_i^T \mathbf{F}_i)}{3} \geq 1$$

and the deviatoric velocity gradient is

$$\bar{\mathbf{L}} = \mathbf{L} - \frac{\text{Tr}(\mathbf{L})}{3} \mathbf{I}$$

(13)

#### 4.1.3 \*MAT\_SIMPLIFIED\_JOHNSON\_COOK

The Johnson-Cook material model is an elastic-plastic constitutive equation. Its advantage is a simple empirical implementation of strain, strain rate, and heat-dependent plasticity. There are several polymers in the WIAMan that behave as hard plastics, showing a linear, rate-independent stress-strain relationship in the small-strain elastic range followed by rate-dependent yielding behavior in the larger strain ranges. The LS-DYNA simplified Johnson-Cook model<sup>22</sup> saves computational time by stripping the thermal effects away from the original Johnson-Cook equation, leaving only the strain hardening and strain-rate scaling components for calculation of flow stress shown in the following equations:

$$\sigma_f = (A + B \bar{\epsilon}_p^n) (1 + c \ln \dot{\epsilon}^*), \quad (14)$$

$$\text{normalized effective strain rate: } \dot{\epsilon}^* = \frac{\dot{\epsilon}}{\dot{\epsilon}_0}, \quad (15)$$

where A is the initial yield stress of the material; B and n are material constants that account for strain hardening; and c is a material constant for strain-rate scaling. The strain rate used in the scaling is normalized by the quasistatic threshold strain rate,  $\dot{\epsilon}_0$ , commonly the lowest strain rate for which material data were provided, but sometimes tuned to provide for the best match to material data.

#### 4.1.4 \*MAT\_BLATZ-KO\_RUBBER

The Blatz-Ko model is a simple hyperelastic constitutive equation commonly used to represent rubber materials. The LS-DYNA implementation fixes the Poisson's Ratio,  $\nu$ , at 0.463 to represent a nearly incompressible rubber,<sup>22</sup> leaving the user only the shear modulus,  $G$ , as a necessary input to the model. Cauchy stress is computed using the left Cauchy-Green strain tensor,  $\mathbf{B}$ , and the determinant of the deformation gradient,  $J$ :

$$\boldsymbol{\sigma} = G \left( \frac{1}{J} \mathbf{B} - J^{-\frac{1}{1-2\nu}} \mathbf{I} \right). \quad (16)$$

#### 4.2 Polymer Fitting Procedure

---

Generally, the first attempt at material fitting of the soft polymers was the BB model. The BB formulation has the advantage of being truly viscoplastic, accounting for rate dependence beyond the elastic realm.<sup>23</sup> Its accuracy has also been demonstrated for a number of engineering rubbers and softer biomaterials.<sup>23</sup> The material model is based upon a micromechanics approach to polymer systems, so soft polyurethane materials such as the various flesh models in WIAMan fit readily into the BB material template. However, as in the case of the 75 Shore A butyl rubber, the BB model had a difficult time conforming to the experimental data provided. For this situation, we turned to the Ogden + Prony Series model. This viscoelastic model bases itself upon empirical high-order polynomial fits and is thus readily adaptable to many curve shapes. As shown in Fig. 15, the Ogden + Prony Series model is able to accurately capture the rate-dependent behavior of the butyl rubber, while BB falls short.

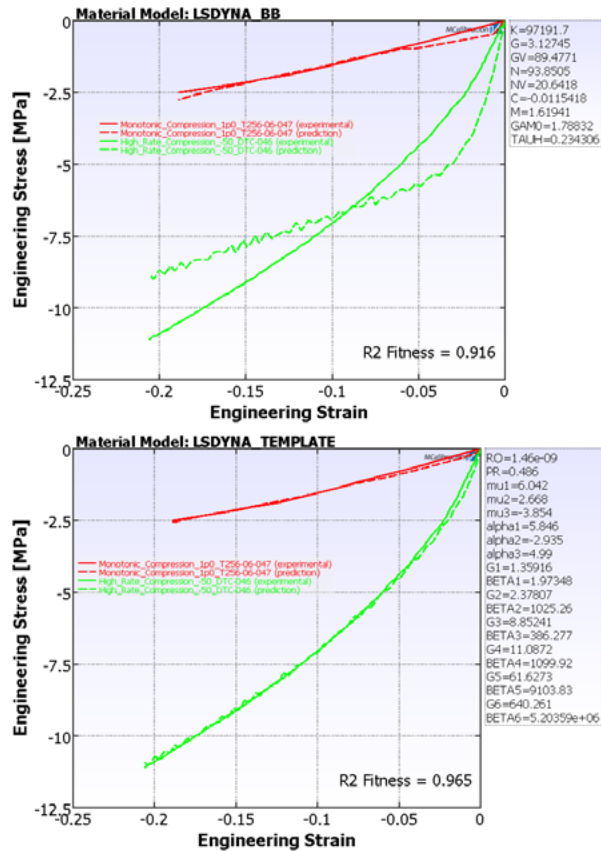


**Fig. 15 BB fit for butyl rubber (top) vs. Ogden+Prony fit (bottom) at strain rates of  $1 \text{ s}^{-1}$  (red) and  $50 \text{ s}^{-1}$  (green)**

There were also situations during the development of this model where LS-DYNA seemed to be less stable while using the BB model in confined areas during higher loading conditions, such as the strength-of-design (SoD) load case. This may be attributed to the contact algorithms exciting the material into a frenzied state. In some situations, such as in the foot flesh, switching the material formulation from BB to Ogden + Prony can help to stabilize the solution. While the Ogden + Prony model may provide a more stable solution, it is decidedly less accurate than the BB model, as shown in Fig. 16. In this figure, the simulated right tibia and calcaneus forces are compared to experimental data for 2 loading conditions, a severe SoD loading case and a low intensity target input (WH1a) for subinjurious UBB loading.<sup>24</sup> For the SoD case, the ATD was subjected to 18-m/s impact velocity and for the WH1a case, the ATD was subjected to 4-m/s impact velocity.

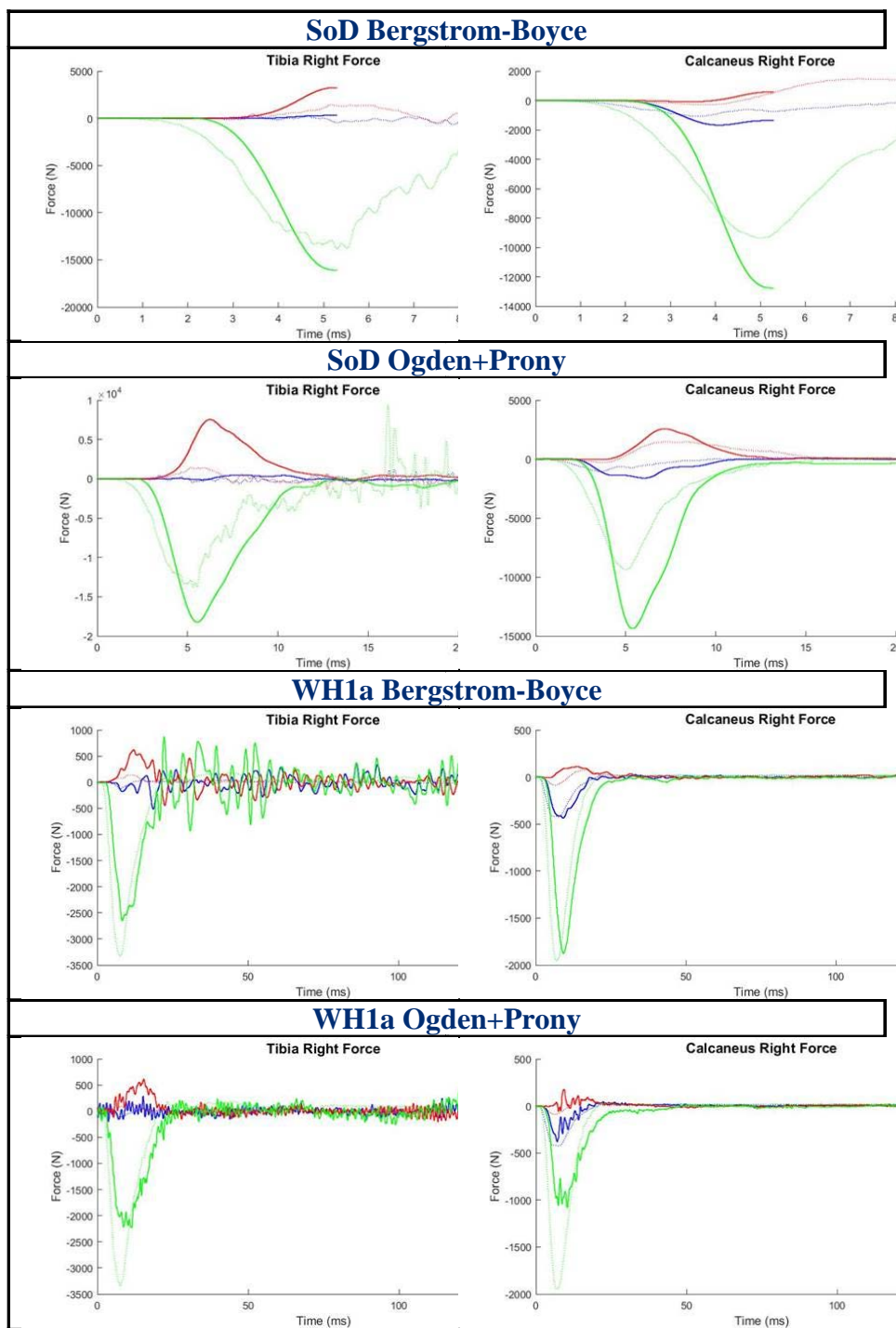


**Fig. 16** Performance results of the tibia and calcaneus load cells during SoD and WH1a load cases using different foot flesh material models

#### 4.2.1 MCalibration Software

For most of the polymer materials, Veryst's MCalibration material fitting software<sup>25</sup> was used to fit the material model variables to experimental data.<sup>23</sup> By default, the software uses an internal FEM solver to apply experimental strain-time history to a single FE, comparing the computed element stress response to the experimental stress response while iterating upon the material variables. Since the BB and Johnson-Cook models come preloaded into MCalibration, this is the method used to compute them.

For material models that are not preloaded into MCalibration (e.g., Ogden with an added Prony Series, the software has the option for users to add other LS-DYNA material models and solve them with the LS-DYNA solver). For this process, MCalibration inserts the strain-time history of the loaded experimental results into a LS-DYNA input file that includes commands to run a single-element test, similar to the way its own default solver operates. MCalibration inserts new material information for each optimization iteration into the LS-DYNA input deck and submits it to the LS-DYNA solver, retrieving the results and comparing them to the experimental stress history.

The default optimization process for MCalibration uses several different optimization schemes including an initial random search followed by Levenberg-Marquardt, NEWUOA, Nelder-Mead Simplex, genetic algorithm, and others.<sup>25</sup> The optimization schemes are cycled until a converged solution is found, a maximum run time is reached, or the user manually ends the run. The default fitness score used to determine quality and convergence is the normalized mean absolute difference (NMAD):

$$NMAD = \frac{\langle |\sigma_{pred} - \sigma_{exp}| \rangle}{\langle |\sigma_{exp}| \rangle}. \quad (17)$$

While NMAD is used by the program as a means to evaluate the fit during the optimization process, a more recognizable curve fitness value is shown on the plotted results, the coefficient of determination or  $R^2$  value, for which a value of 1.0 would represent an exact match to experimental data:

$$R^2 = 1 - \frac{\sum_{i=1}^n (\sigma_i^{pred} - \sigma_i^{exp})^2}{\sum_{i=1}^n (\sigma_i^{exp} - \langle \sigma^{exp} \rangle)^2}. \quad (18)$$

Note that  $\langle \sigma \rangle$  indicates the arithmetic mean of the values contained in vector  $\sigma$  and  $|\sigma|$  indicates the magnitude of each value contained in vector  $\sigma$ .



#### **4.2.2 LS-OPT Software**

Another program available for material fitting operations is LSTC's LS-OPT program. LS-OPT was created as a general-purpose optimization program for LS-DYNA. Among LS-OPT's features is a curve mapping algorithm designed with material fitting in mind. For models that have difficulty fitting in MCalibrate (e.g., Delrin in the WIAMan material library), LS-OPT provides another robust option that uses LS-DYNA as its base FEM solver. A modeler builds and submits a fully functional LS-DYNA model and tags features of the model for LS-OPT to set as variables in its optimization. Material variables are marked in the LS-DYNA input deck and LS-OPT approaches the problem by either direct simulation via a genetic algorithm (GA) or building a metamodel from strategically chosen points in the variable design space. The GA approach was selected for finding the properties of the Delrin material model, since it proved very robust when certain combinations of variables in the design space caused simulations to fail before completion.

GAs approach the problem in much the same way as biological genetic evolution, optimally sampling the design space to create a starting set, and then selecting the fittest of the group to combine attributes and act as parents of a new generation of samples. A probability of mutation creates the ability for random variation to occur within the generations without influence from the fittest samples of the previous generation. The method is robust, but can be time consuming with large or long-running models since many individual simulations must be run to converge upon a solution. Since the simulations for material fitting only included 8-element models, running many simulations was not a barrier to the solution.

The Delrin fitting solution was approached with an 8-element block instead of the usual single-element simulation. The fit solution was unstable for this particular material when only one element was used in the optimization process; switching to LS-OPT using multiple elements solved this problem.

#### **4.2.3 Molded Neck Rubber Fit Procedure**

The molded neck rubber received its own fit procedure. Material characterization data were not available; however, isolated WIAMan neck experiments had been performed at Duke University. Replicating the Duke experimental setup in a LS-DYNA FEM, a team at the Wake Forrest Center for Injury Biomechanics optimized the shear modulus of a Blatz-Ko model (Table 20) to fit the force-time histories between the model and the experiment.

**Table 20 Blatz-Ko fit parameters for select WIAMan polymers**

Material Library ID	Name	Use	$\rho$ (kg/m <sup>3</sup> )	G (MPa)
23	Black Natural Rubber 70 Shore A	shoulder stops	930	3.45
25	Black Neoprene Rubber 65 Shore A	arm stops	1,230	2.64
26	Black Neoprene Rubber 80 Shore A	elbow compression washers	1,230	5.94
27	Black Neoprene Rubber 40 Shore A	elbow and knee stops	1,230	0.68
32	Tan Polyurethane 70 Shore D	leg DAS covers	1,140	51.69
36	Black SBR Rubber 75 Shore A	upper leg absorber washer	940	4.53
48	Euro Brown Urethane 80 Shore A	upper arm "Z" stop	1,070	5.94
49	Euro Brown Urethane 95 Shore A	lower leg stops; elbow pin washers	1,130	10.20
51	Polyurethane Skull 75 Shore D	skull	1,140	67.75
67	Optimized Molded Neck Rubber 45 Shore A	molded neck	1,180	1.96
975	Left Boot Tread Rubber	boot tread	1000	15
983	Right Boot Tread Rubber	boot tread	1000	15

### 4.3 Polymer Fitting Results

#### 4.3.1 Butyl Rubber 75 Shore A Compliant Elements and Spine Rubber

This material was fit to the native LS-DYNA Ogden rubber model with viscoelastic Prony Series (Table 21 and Fig. 17). The characterization data were obtained from Veryst and the software MCalibrate was used to fit the characterization data to the material model. A material model provided by Corvid was used as a basis for MCalibrate to further tune the constitutive properties to LS-DYNA's Ogden model.

**Table 21 Butyl rubber 75 Shore A material parameters**

$\rho$ (kg/m <sup>3</sup> )	$\nu$	$\mu_1$ (MPa)	$\mu_2$ (MPa)	$\mu_3$ (MPa)	$\alpha_1$	$\alpha_2$	$\alpha_3$
1460	0.486	6.042	2.668	-3.854	5.846	-2.935	4.99
$G_1$ (MPa)	$G_2$ (MPa)	$G_3$ (MPa)	$G_4$ (MPa)	$G_5$ (MPa)	$G_6$ (MPa)		
1.3592	2.3781	8.8524	11.0872	61.6273	640.2614		
$\beta_1$ (1/s)	$\beta_2$ (1/s)	$\beta_3$ (1/s)	$\beta_4$ (1/s)	$\beta_5$ (1/s)	$\beta_6$ (1/s)		
1.9735	1025.2649	386.2772	1099.9231	9103.8316	5203539		

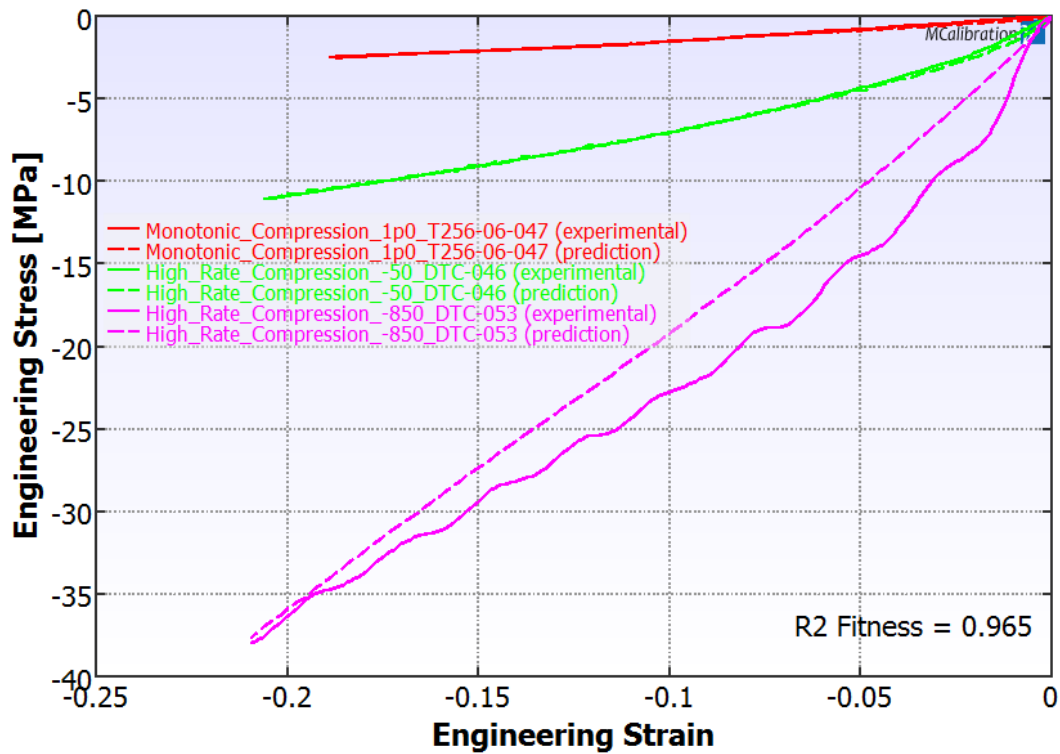


Fig. 17 Butyl rubber 75 Shore A material fit

#### 4.3.2 Proflex 30 Polyurethane Pelvis Flesh

This material was fit to the native LS-DYNA BB model (Table 22 and Fig. 18). The material characterization and fitting were performed by Veryst.

Table 22 Pelvis flesh material parameters

$\rho$ (kg/m <sup>3</sup> )	K (MPa)	G (MPa)	$G_v$ (MPa)	n	$n_v$
1035	10	0.3298	0.03944	17.6804	2.7016
C	m	$\gamma_0$ (s)	$\tau_h$ (s)		
-0.37317	2.37689	1	0.1367		

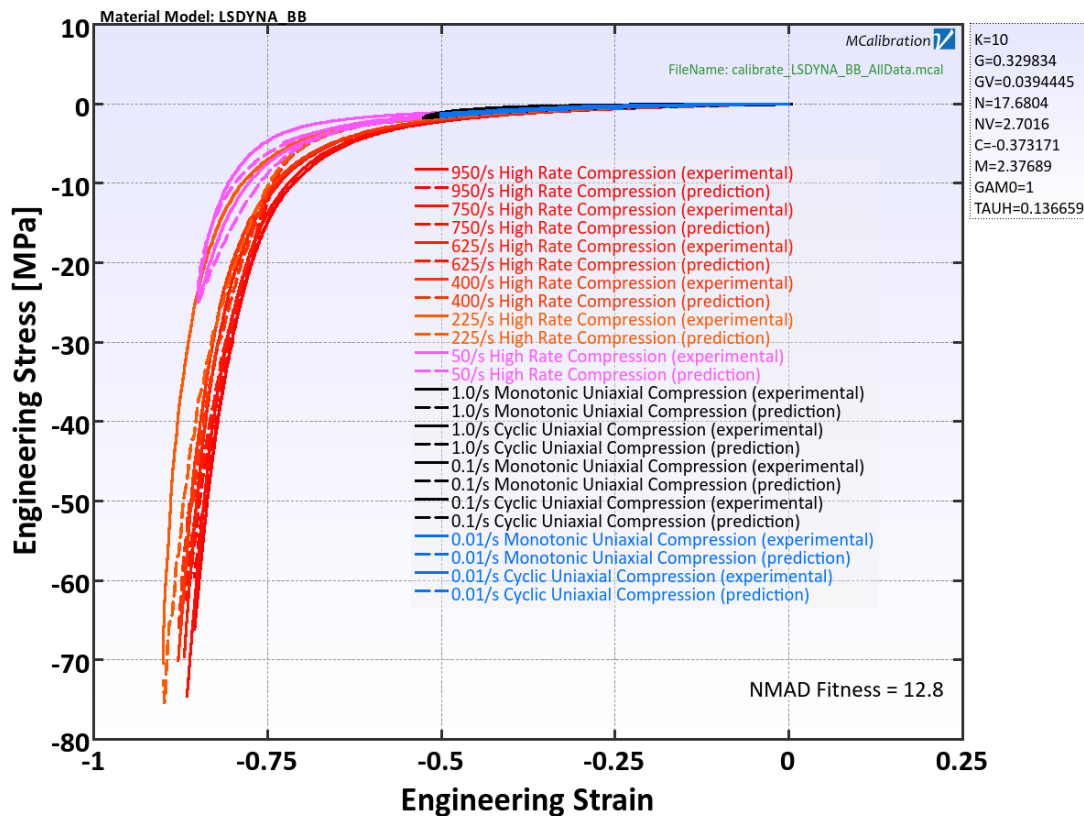


Fig. 18 Pelvis flesh material fit

#### 4.3.3 E1030AL Polyurethane Arm, Leg, and Abdomen Flesh

This material was fit to the native LS-DYNA BB model (Table 23 and Fig. 19). The characterization data were obtained from Veryst and the software MCalibrate was used to fit the characterization data to the material model.

Table 23 Arm, leg, and abdomen flesh material parameters

$\rho$ (kg/m <sup>3</sup> )	K (MPa)	G (MPa)	G <sub>v</sub> (MPa)	n	n <sub>v</sub>
1050	10	0.40045	0.79822	39.407626	49.731324
C	m	$\gamma_0$ (s)	$\tau_h$ (s)		
-1.1395535	1.3164482	1	0.091117		

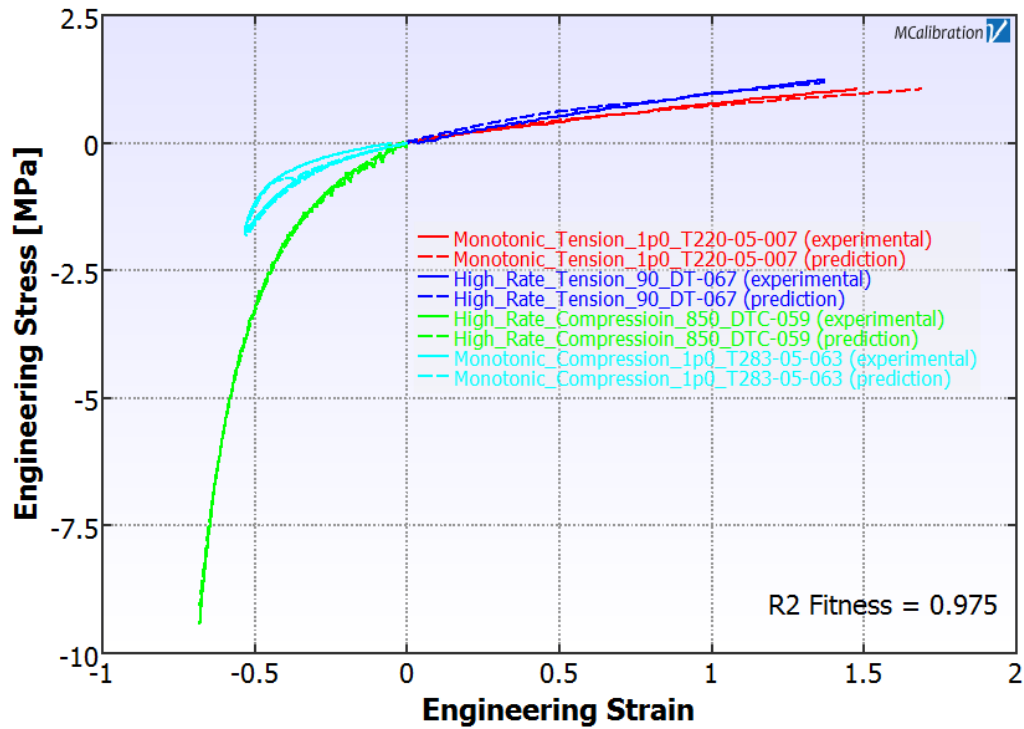


Fig. 19 Arm, leg, and abdomen flesh material fit

#### 4.3.4 XE1031 Polyurethane Foot Flesh

This material was fit to the native LS-DYNA Ogden rubber model with viscoelastic Prony series (Table 24 and Fig. 20). The characterization data were obtained from Veryst and the software MCalibrate was used to fit the characterization data to the material model.

Table 24 Foot flesh material parameters

$\rho$ (kg/m <sup>3</sup> )	$\nu$	$\mu_1$ (MPa)	$\mu_2$ (MPa)	$\mu_3$ (MPa)	$\alpha_1$	$\alpha_2$	$\alpha_3$
1063	0.4	1.0652	0.0013381	0.22052	1.4941506	11.399695	-1.224465
$G_1$ (MPa)	$G_2$ (MPa)	$G_3$ (MPa)	$G_4$ (MPa)	$G_5$ (MPa)			
0.016304	0.11873	0.20649	0.72263	0.035175			
$\beta_1$ (1/s)	$\beta_2$ (1/s)	$\beta_3$ (1/s)	$\beta_4$ (1/s)	$\beta_5$ (1/s)			
101.7071	1044.1123	1045.9716	1211.4211	11002.213			

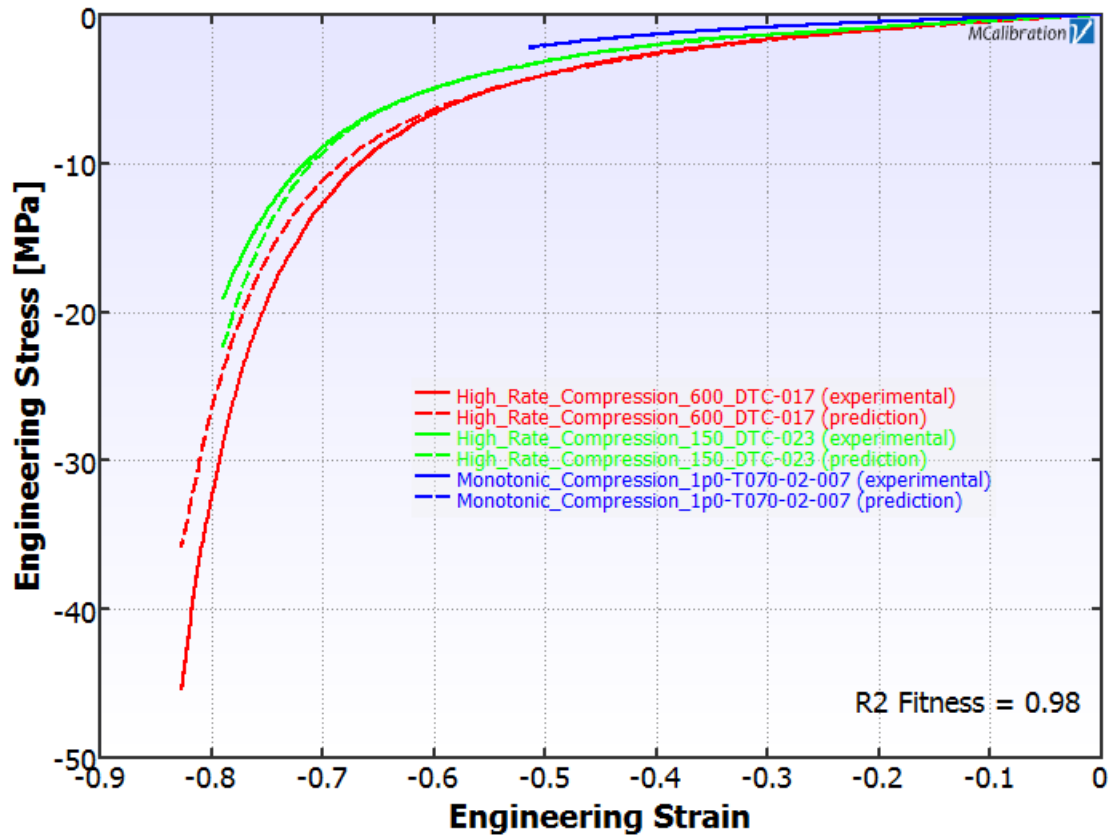


Fig. 20 Foot flesh material fit

#### 4.3.5 FD70 Polyurethane Foot Plate

This material was fit to a Johnson-Cook model (Table 25 and Fig. 21). The characterization data were obtained from Veryst and the software MCalibrate was used to fit the characterization data to the material model.

Table 25 Foot plate material parameters

$\rho$ (kg/m <sup>3</sup> )	E (MPa)	$\nu$	$\nu_p$	$\epsilon_0$ (s)
1210	600.2922	0.35	1.0	1.9352
A (MPa)	B (MPa)	n	C	
20.9541	96.1332	0.791049	0.18333	

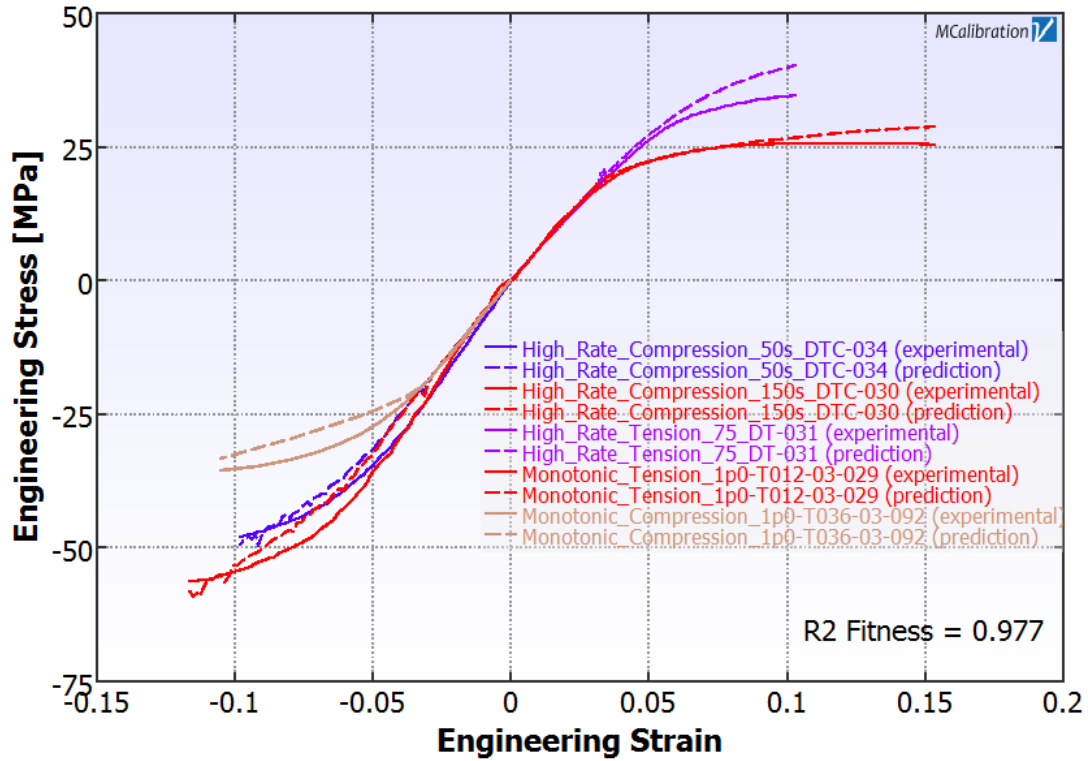


Fig. 21 Foot plate material fit

#### 4.3.6 Delrin Calcaneus Cap

This material was fit to the native LS-DYNA Simplified Johnson-Cook model (Fig. 22 and Table 26). The characterization data were obtained from Veryst and the software LS-OPT was used to fit the characterization data to the material model.

Table 26 Calcaneus cap material parameters

$\rho$ (kg/m <sup>3</sup> )	E (MPa)	$\nu$	$\nu_p$	$\epsilon_0$ (s)
1410	2543.45	0.35	1.0	1.4229
A (MPa)	B (MPa)	n	C	
39.5381	85.0114	1.53765	0.189606	

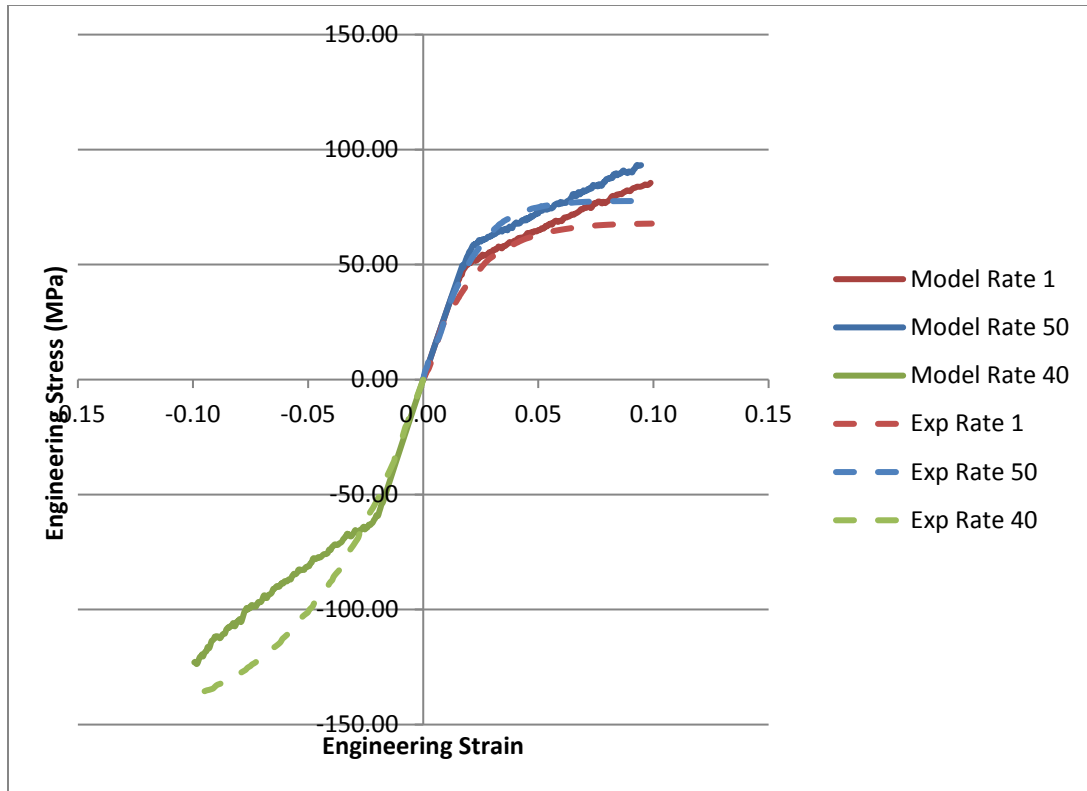


Fig. 22 Calcaneus cap material fit

#### 4.3.7 TC892 Polyurethane Pelvic Bone

This material was fit to a Johnson-Cook model (Fig. 23 and Table 27). The characterization data were obtained from Veryst and the software MCalibrate was used to fit the characterization data to the material model.

Table 27 Pelvis bone material parameters

$\rho$ (kg/m <sup>3</sup> )	E (MPa)	$\nu$	$\nu p$	$\epsilon_0$ (s)
1160	1924.4343	0.4	0.0	1.0655
A (MPa)	B (MPa)	n	C	
53.8458	98.7793	0.3581026	0.0688742	



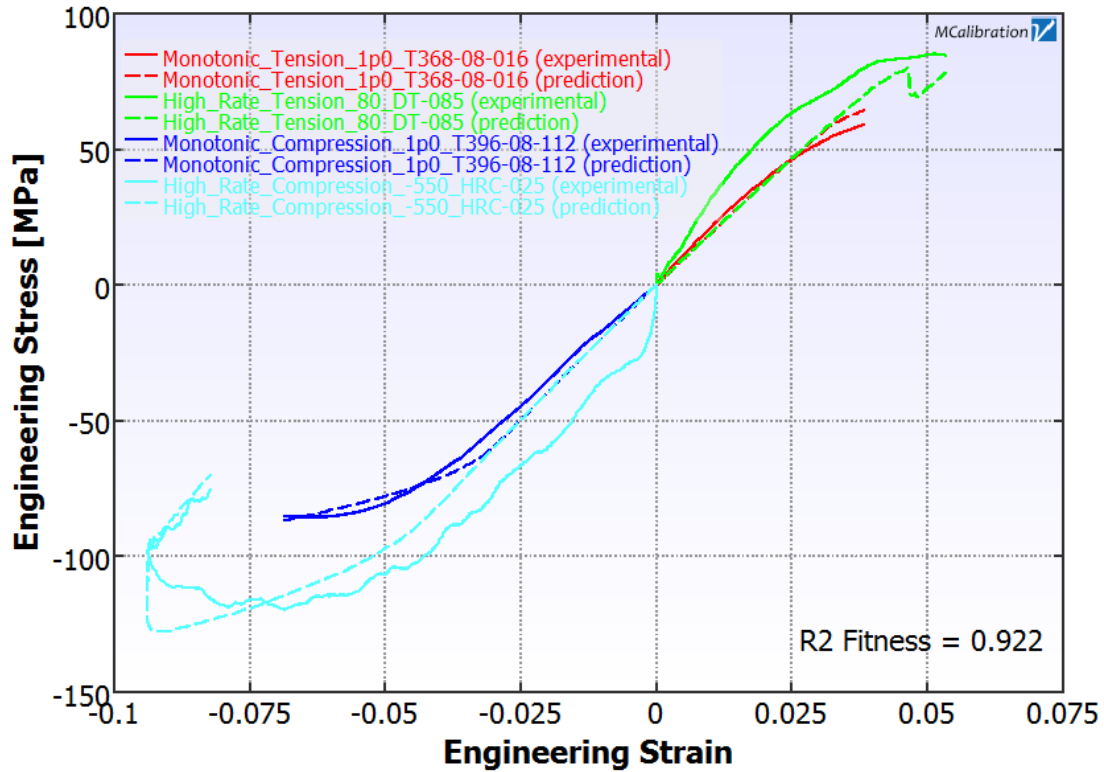


Fig. 23 Pelvis bone material fit

#### 4.3.8 Rencast 6425 Polyurethane Tailbone

This material was fit to a Johnson-Cook model (Fig. 24 and Table 28). The characterization data were obtained from Veryst and the software MCalibrate was used to fit the characterization data to the material model.

Table 28 Tailbone material parameters

$\rho$ (kg/m <sup>3</sup> )	E (MPa)	$\nu$	$\nu_p$	$\epsilon_0$ (s)
1180	716.8913	0.46	1.0	1.2861
A (MPa)	B (MPa)	n	C	
21.5051	22.4628	0.3478949	0.136802	

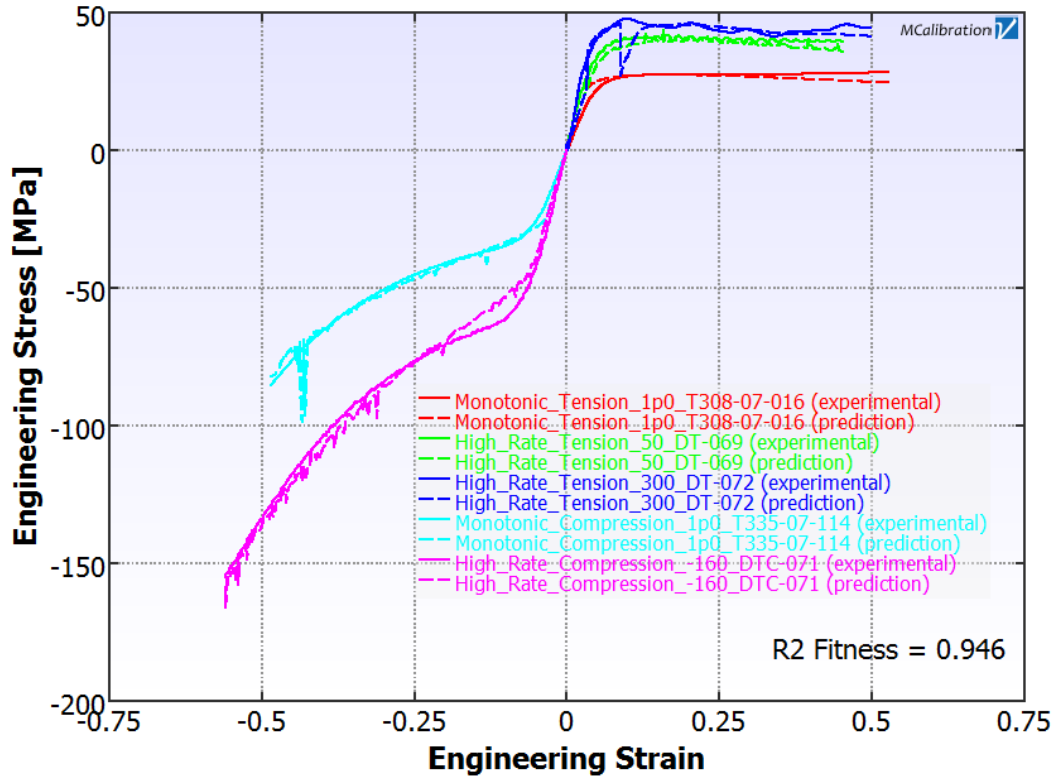


Fig. 24 Tailbone material fit

#### 4.3.9 ISODAMP Heel Plug

This material was fit to the native LS-DYNA Ogden rubber model with viscoelastic Prony series (Fig. 25 and Table 29). The characterization data were obtained from ARL and the software MCalibrate was used to fit the characterization data to the material model.

Table 29 Heel plug material parameters

$\rho$ (kg/m <sup>3</sup> )	$\nu$	$\mu_1$ (MPa)	$\mu_2$ (MPa)	$\mu_3$ (MPa)	$\alpha_1$	$\alpha_2$	$\alpha_3$
1290	0.49	0.4327	0.55538	-0.5700	-1.183380	-0.689722	-4.974810
$G_1$ (MPa)	$G_2$ (MPa)	$G_3$ (MPa)	$G_4$ (MPa)	$G_5$ (MPa)			
0.46338	0.093381	0.0060828	1.6867	123.874			
$\beta_1$ (1/s)	$\beta_2$ (1/s)	$\beta_3$ (1/s)	$\beta_4$ (1/s)	$\beta_5$ (1/s)			
0.57718	777.275	435.748	1248.84	23248.699			

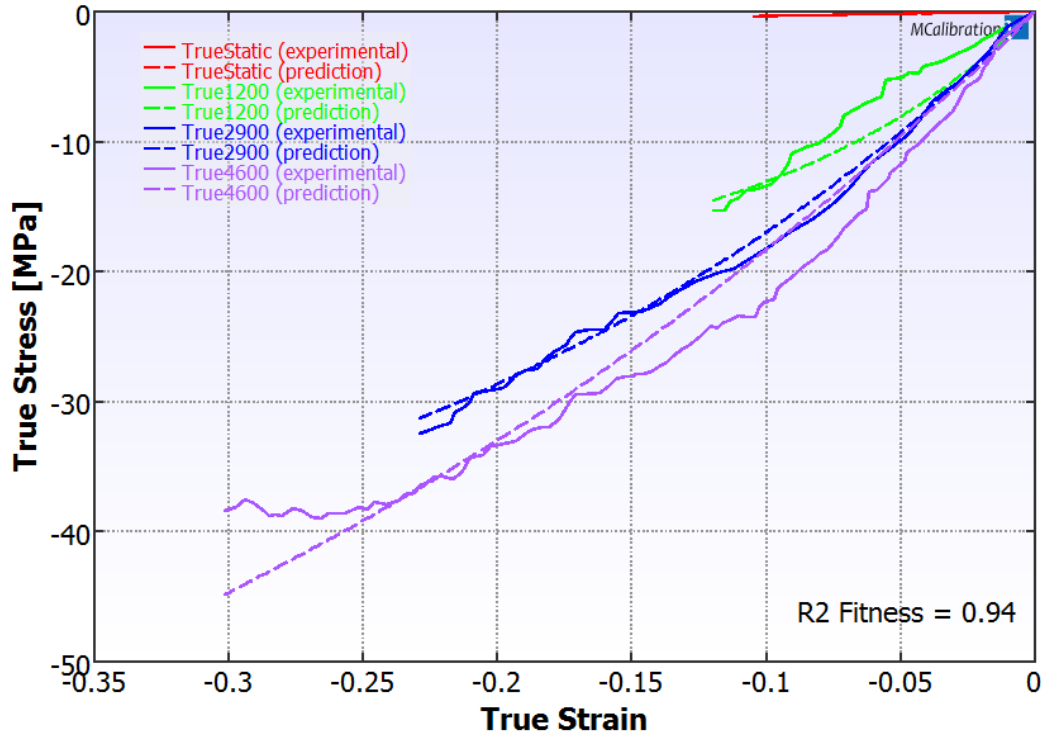


Fig. 25 Heel plug material fit

## 5. Typical WIAMan Strain Rate Environment

As mentioned previously, material models developed by both teams used available strain-rate test data ranging from quasistatic to 1,000 strain/s (where s is second), when applicable, in their material model parameters extraction algorithms. Simulation results indicated that the inclusion of very high-strain-rate effects (above 150 strain/s) was more than adequate for the WIAMan ATD modeling since typical strain rates in WIAMan model simulations did not exceed 150 strain/s. Materials for the TD were tested at higher rates based on estimated strain rates reported for Hybrid 3 simulations by Malone.<sup>26</sup> Future testing of new polymeric materials for the next-generation ATD could be tested at a much lower strain rates than 1,000 strain/s given no changes in the WIAMan loading environment.

Figures 26–28 show the strain-rate data from 2 whole-body simulations of the ATD tests due to vertical accelerative loading. Details of the test configurations for the whole-body tests and simulation results are available in the literatures.<sup>6,7</sup> The whole-body test results came from the APL VALTS tests that impacted the seat and the floor at prescribed velocity profiles associated with a peak velocity and a time to peak (TTP) based on the target input conditions for subinjurious UBB loadings used for the WIAMan biomechanical research investigations. The first simulation

(Fig. 26) was from WH1a level tests in which the ATD with no personal protective equipment [PPE]) was tested at the APL VALTS for a loading profile having an amplitude of 4 m/s at a 5-ms TTP. Both floor, and seat were subjected to the amplitude and the TTP with different loading profiles discussed in the simulation results section. Figures 27 and 28 show the strain-rate data extracted from WH2a (without PPE) and WH2b (with PPE) level tests, for a peak velocity of 6 m/s at a 5-ms TTP floor, and 4 m/s at a 10-ms TTP seat. PPE included helmet, body armor vest, and boot. Further details of the whole-body test conditions and the associated results are available in literature by Pietsch et al.<sup>24</sup> All materials were fit to their models within this range, many including data well beyond 150 strain/s, and are thus relevant for both typical and extreme load cases. As indicated in Figs. 27 and 28, a maximum strain rate of 150 strain/s was observed in the heel flesh for both test conditions.

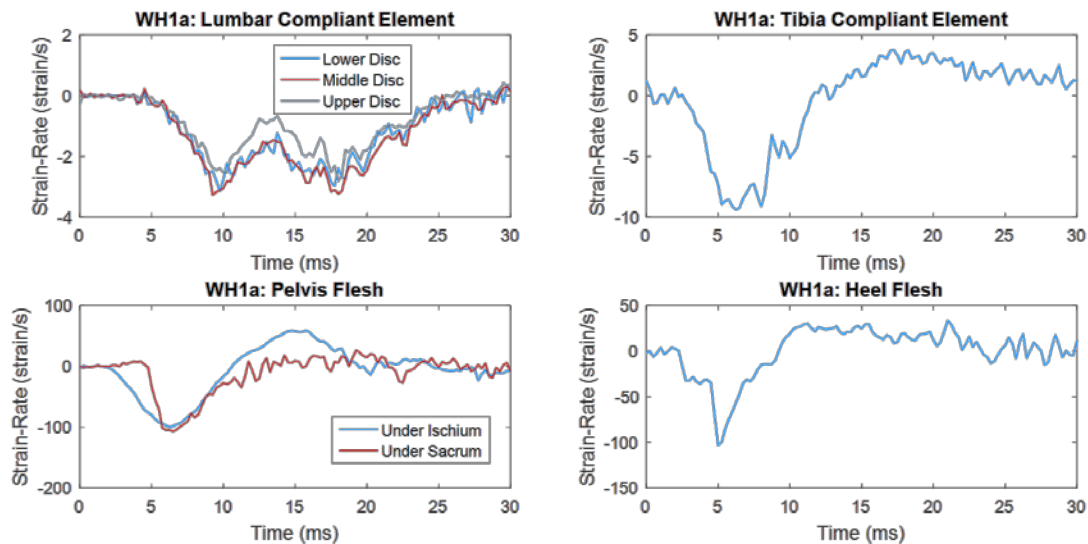


**Fig. 26** Strain rates experienced by soft polymers during the VALTS test at WH1a levels (4 m/s at a 5-ms TTP floor, and seat, no PPE)

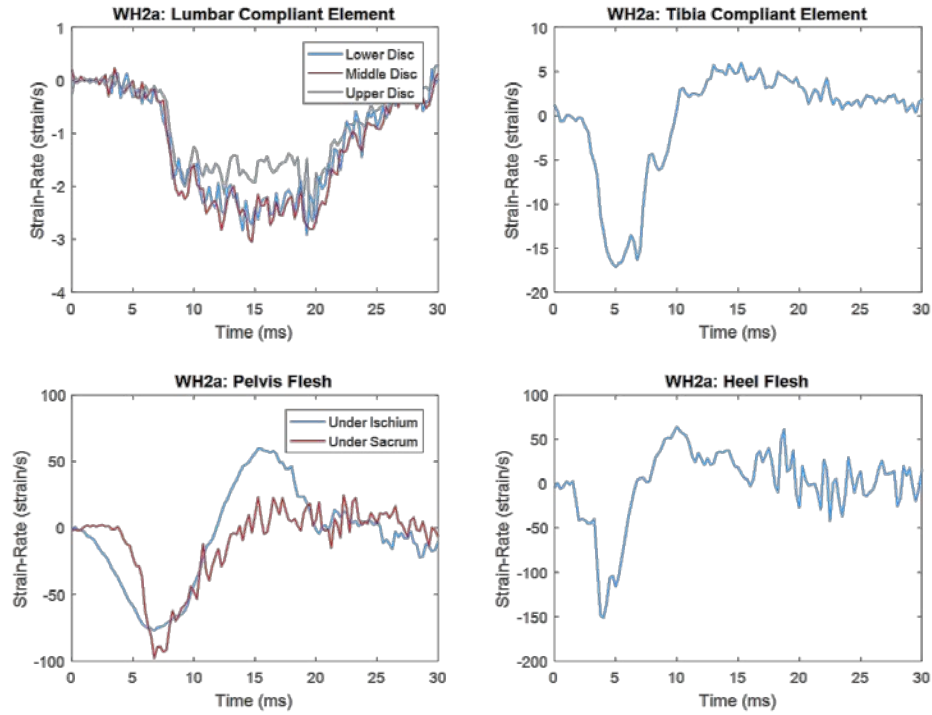


**Fig. 27** Strain rates experienced by soft polymers during the VALTS test at WH2a levels (6 m/s at a 5-ms TTP floor, 4 m/s at a 10-ms TTP seat, no PPE)

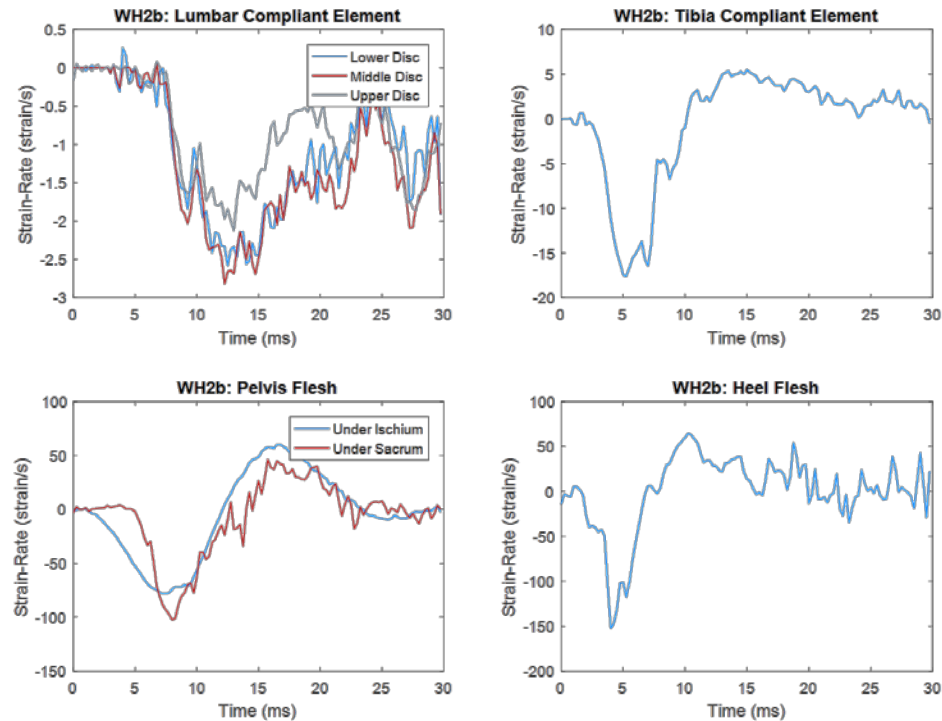


**Fig. 28** Strain rates experienced by soft polymers during the VALTS test at WH2b levels (6 m/s at a 5-ms TTP floor, 4 m/s at a 10-ms TTP seat, with PPE)

## 6. Whole-Body ATD Model Simulation Results

---

Illustrative examples of the system-level, whole-body model performance of the material models described previously—by both modeling teams—are presented. The whole-body ATD experimental tests data came from the APL VALTS. The VALTS is a vertical impact allowing laboratory testing of various UBB loading profiles and scenarios. The system is capable of independent loading of the legs and pelvis of a seated ATD. Input loads were characterized by the peak velocity and TTP of the floor and seat independently. Total mass of the WIAMan TD FE model was 79.8 kg for the LS-Dyna case and 83.88 kg for the Velodyne model compared to the mass of the physical prototype of 82.7 kg, which included external sensor wiring not present in the model.

The physical WIAMan TD with boots was tested experimentally at different impact velocities on the uncushioned VALTS rig. System validation was based on experimental testing and paired simulations of the WIAMan for the following conditions:

- WH1a = 4 m/s at 5 ms TTP floor, 4 m/s at 5 ms TTP seat, no PPE

Several repeat tests at each velocity were run to investigate repeatability, but only a single case from each test series was used for validation. The WH1A condition is the lower velocity of the 2 cases yet with shorter TTP velocities, where the table (to which the throne is mounted) is driven to 4.5 m/s at 5 ms TTP and the floor reached 4.1 m/s at 4 ms TTP. The velocity histories were captured in test via a hard mount accelerometer on the table and floor plates, respectively, and subsequently integrated into velocity histories. The velocity boundary conditions employed for each simulation are shown in Fig. 29.

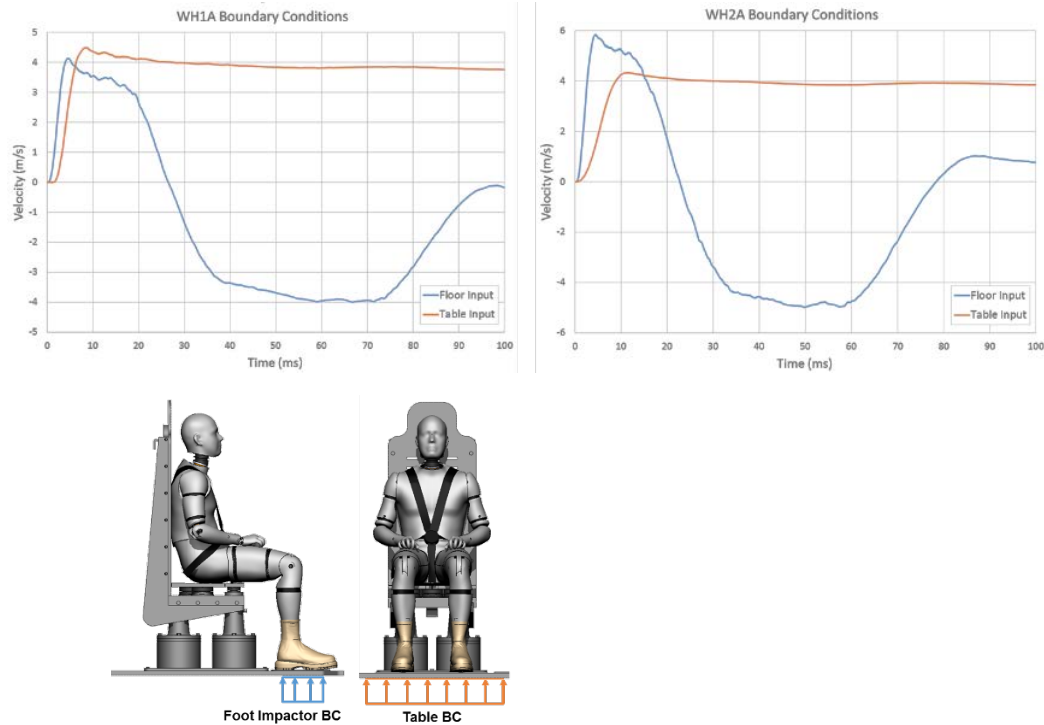


**Fig. 29 Velocity history from the WH1A and WH2A VALTS tests that are employed as the simulation boundary conditions**

Both simulations (LS-DYNA and Velodyne) of the WH1A case were carried out and the computational sensors histories were captured for validation (Figs. 30–34 and Table 30). Response metrics for the over 30 sensors were aggregated using Correlation and Analysis (CORA; version 3.6) to compute a composite score. CORA measures the correlation of simulation versus test responses on a scale of 0 to 1, where 0 represents no correlation and 1 represents perfect correlation of response signals. A CFC 600 filter is applied to all force and moment signals and a CFC 1000 filter is applied to all accelerometer signals. Model validation results from the paired tests were compared using CORA, which numerically assesses the magnitude, shape, and phase of similar response signals to obtain objective metrics.<sup>27</sup> Each entry in Table 30 is color coded on a scale from red (a score of 0.0) to green (a score of 1.0). In general, based on average CORA scores of greater than 0.65 in conjunction with the engineering judgement of the WIAMan M&S team, the WIAMan model is considered to be validated for these nominal impact cases.<sup>24</sup>

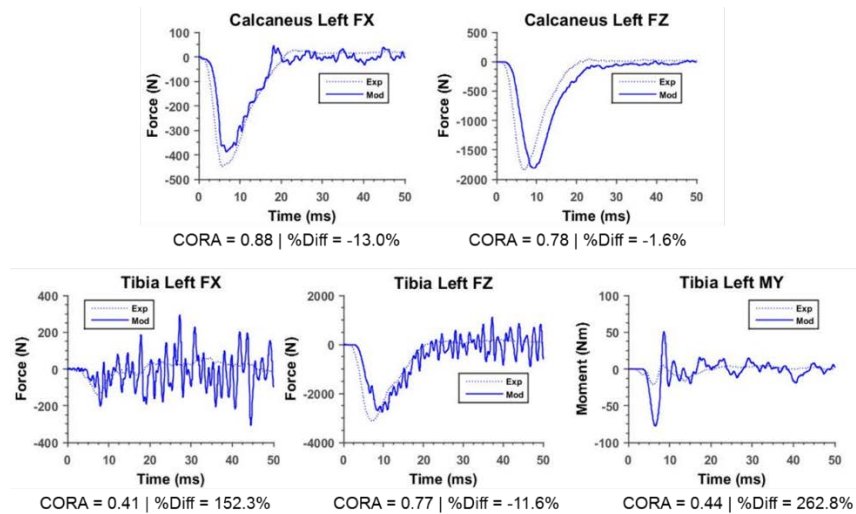


**Fig. 30 Match pair validation results for the lower extremity at the heel and mid-tibia sensor regions for the simulation and the experiment under the WH1a test condition**

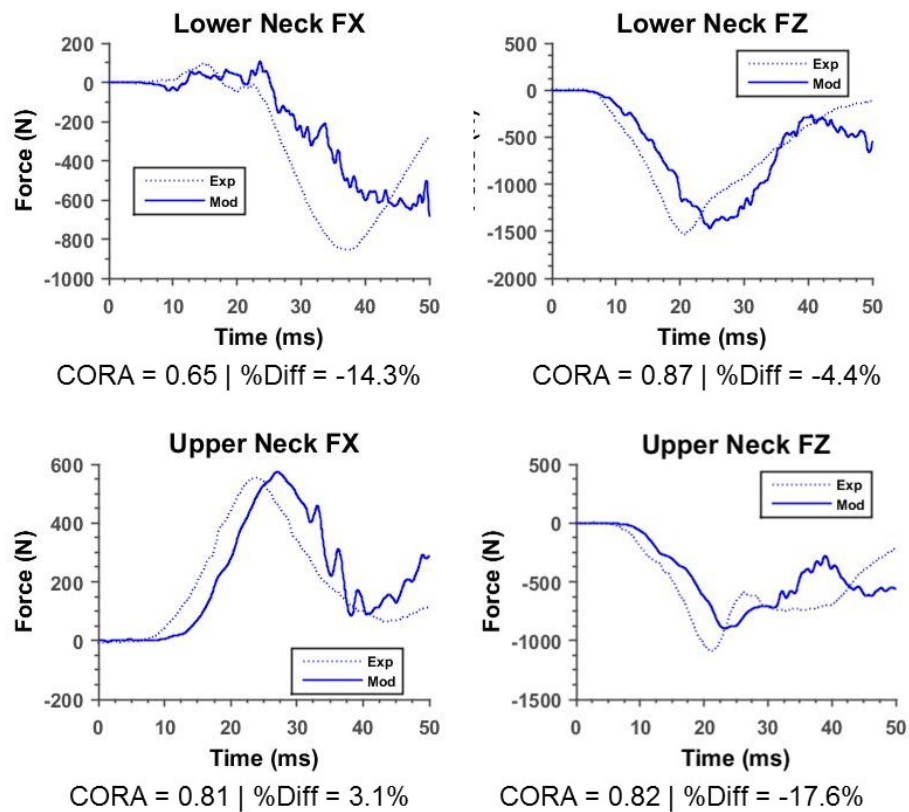


**Fig. 31 Match pair validation results for the lower and upper neck sensor regions for the simulation and the experiment under the WH1a test condition**



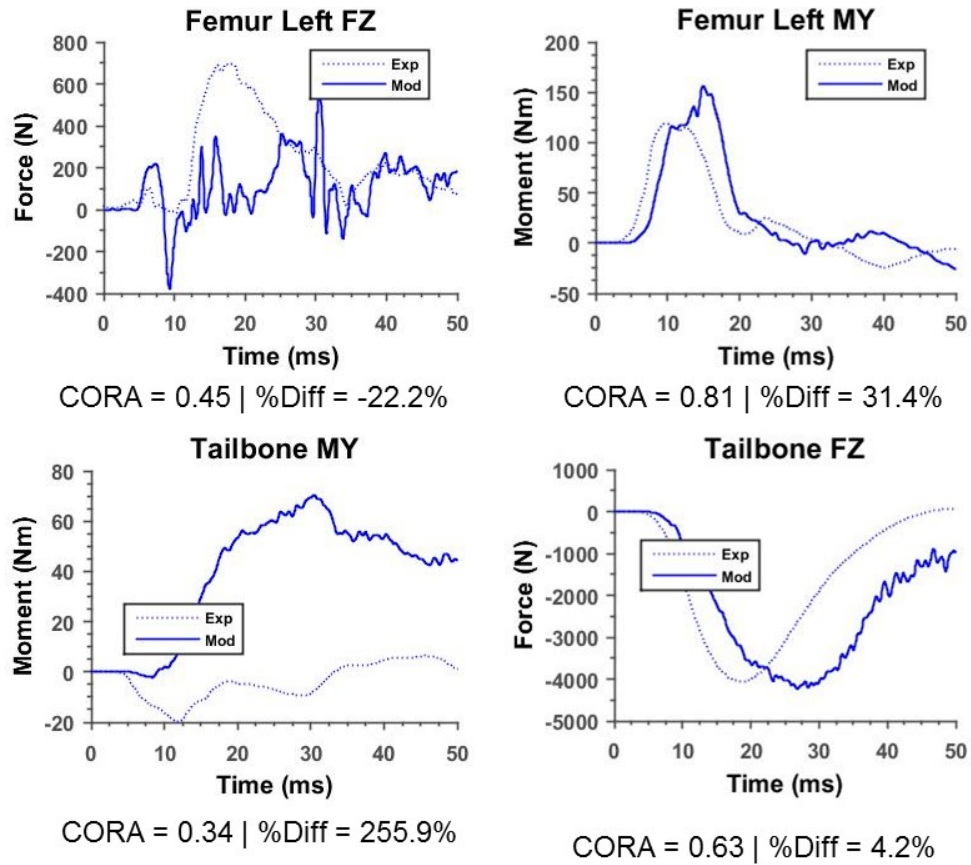


**Fig. 32 Match pair validation results for the lower extremity at the femur and tailbone sensor regions for the simulation and the experiment under the WH1a test condition**

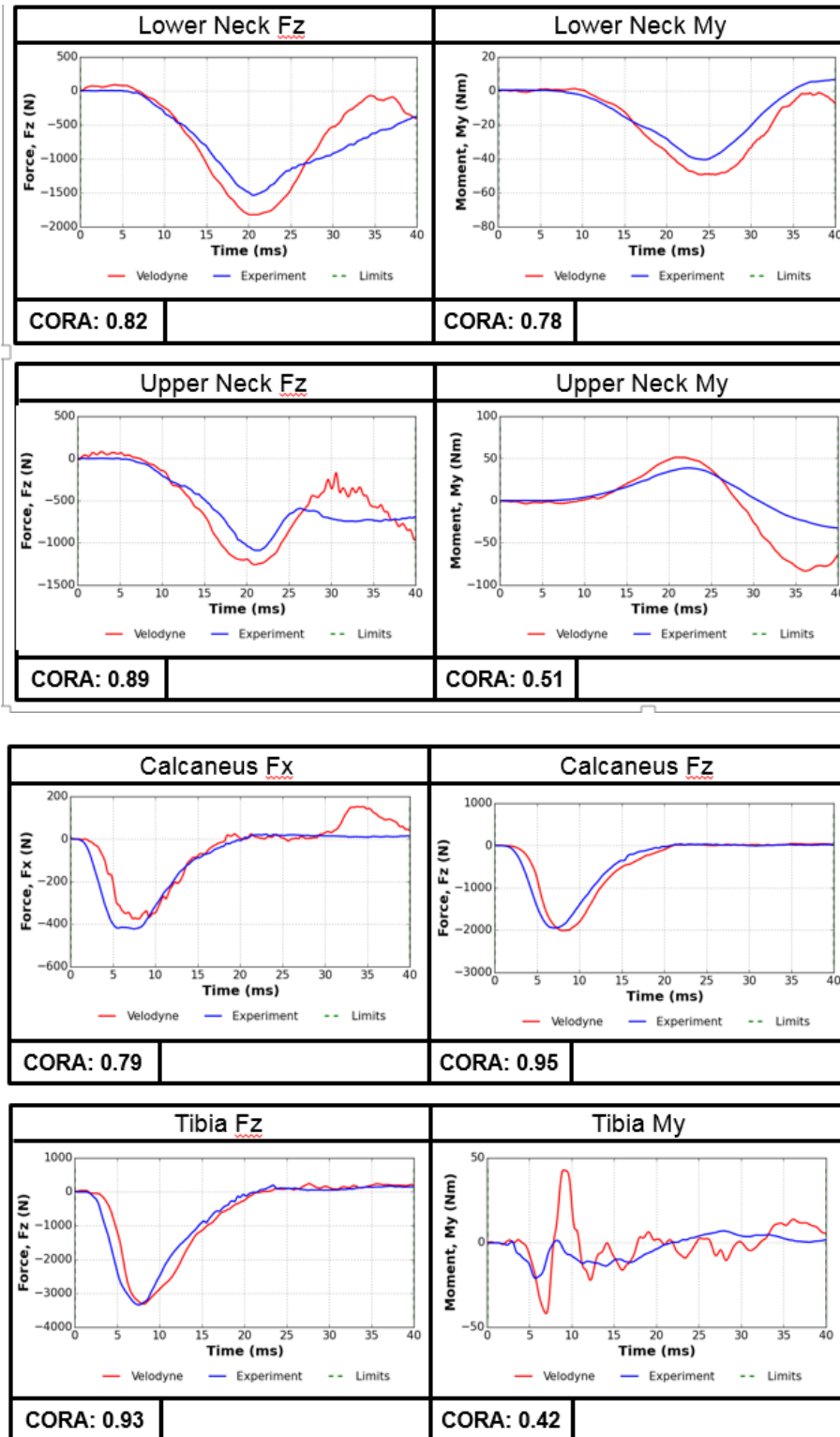


**Fig. 33** Example cross-plots of the Velodyne simulation and test for WH1A (neck calcaneus and tibia)

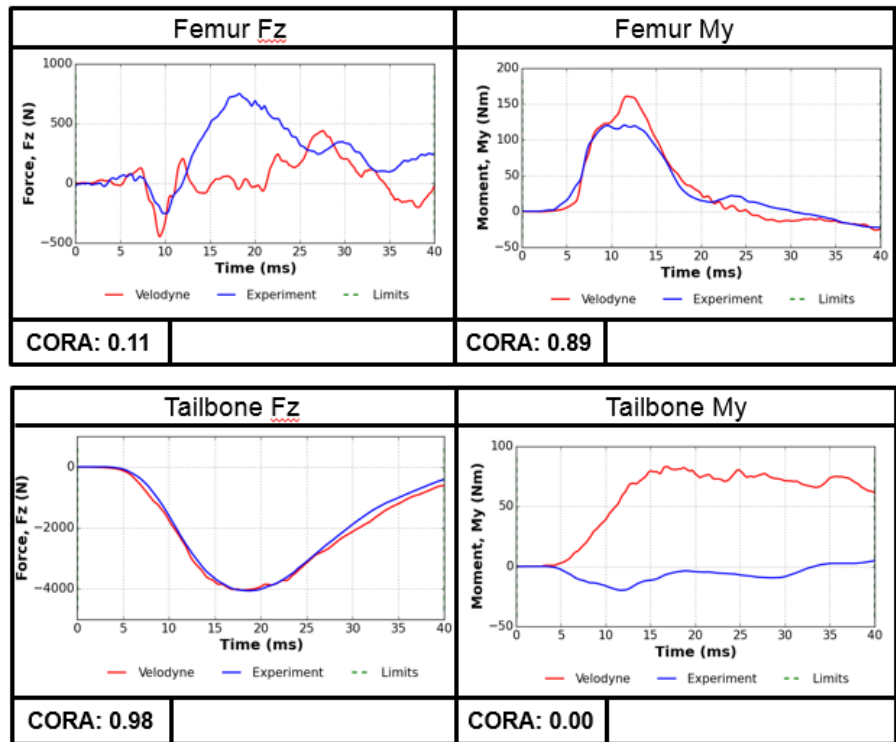


**Fig. 34** Example cross-plots of the Velodyne simulation and test for WH1A (femur and tailbone)

**Table 30 CORA summary table for the WIAMan TD WH1A Velodyne simulations**

## WH1A

Abscissa	Shape	Magnitude	Phase	Total
Calcaneus_Fx	0.761	0.802	0.825	0.796
Calcaneus_Fz	0.995	0.926	0.845	0.922
Tibia_Fx	0.180	0.896	0.809	0.628
Tibia_Fz	0.988	0.978	0.845	0.937
Tibia_My	0.058	0.327	0.898	0.428
Femur_Fx	0.520	0.259	0.677	0.485
Femur_Fz	0.108	0.244	0.000	0.117
Femur_My	0.918	0.750	1.000	0.889
Foot_Az	0.497	0.814	0.877	0.729
Sacrum_Fz	0.993	0.940	1.000	0.978
Sacrum_My	0.000	0.019	0.000	0.006
Pelvis_Ax	0.165	0.227	0.518	0.303
Pelvis_Az	0.634	0.673	0.807	0.705
Pelvis_Rdoty	0.661	0.821	0.986	0.823
Lumbar_Fx	0.160	0.223	0.000	0.128
Lumbar_Fz	0.975	0.730	1.000	0.902
Lumbar_My	0.967	0.276	1.000	0.748
T12L1_Fx	0.883	0.273	0.959	0.705
T12L1_Fz	0.942	0.665	1.000	0.869
T12L1_My	0.005	0.274	0.000	0.093
T5_Fx	0.787	0.505	0.000	0.431
T5_Fz	0.961	0.883	1.000	0.948
T5_My	0.788	1.000	0.614	0.801
LowerNeck_Fx	0.942	0.867	0.611	0.807
LowerNeck_Fz	0.805	0.835	0.836	0.825
LowerNeck_My	0.958	0.586	0.811	0.785
UpperNeck_Fx	0.598	0.782	0.759	0.713
UpperNeck_Fz	0.798	0.867	1.000	0.888
UpperNeck_My	0.646	0.295	0.600	0.514
Head_Ax	0.877	0.372	1.000	0.750
Head_Az	0.454	0.709	0.995	0.719
	<b>0.646</b>	<b>0.607</b>	<b>0.718</b>	<b>0.657</b>

## 7. Conclusions

The material characteristics parameters specific to the 2 FEM codes (LS-DYNA and Velodyne) for 8 polymeric materials used in key components in the WIAMan ATD TD were presented in this report. Both material characterization schemes used the experimentally derived multirate compression and tension material test data from the same source to extract material model parameters for their respective analytical ATD models. Material models were created based on a number of available characteristics models. Typically, an Ogden or BB material model was used for the soft materials. Simulation results indicated that typical strain rates in the WIAMan ATD do not exceed 150 strain/s for typical severe and subinjurious

UBB loadings environment for which the WIAMan ATD has been designed. Future testing of new polymeric materials for the next-generation ATD could be tested at a much lower strain rates than 1,000 strain/s given no changes in the WIAMan loading environment.

The material models were subsequently validated in the subassembly level validation. There is room for improvement in the material model fitting process; however, because of the good comparison (acceptable to a degree that serves the purpose of evaluating the evolving ATD design iterations) of experimental and simulation results for whole-body test cases, the model parameters extracted in the report were deemed appropriate. Intra- and intercomparisons of model simulation results for both FE codes with the identical experimental test cases indicated good correlations. The use of 2 FE codes in solving an identical simulation environment also provided an opportunity to extract two data points for the same simulation environment thus providing an increased degree of confidence in the model predictability. Finally, a brief summary of the whole-body simulation results (both models) of an ATD response due to vertical accelerative loading were compared for the same experimental data to document the predictive capability of material models.

## 8. References

---

1. Warrior Injury Assessment Manikin (WIAMan). Washington (DC): dgMarket; 2016 May 9 [accessed 2016]. <http://www.dgmarket.com/tenders/np-notice.do?noticeId=13763702>.
2. Hoppel C. et al. Workshop on numerical analysis of human and surrogate response to accelerative loading. Aberdeen Proving Ground (MD): Army Research Laboratory (US); 2014 May. Report No.: ARL-SR-287.
3. Prevention, mitigation, and treatment of blast injuries. Ft Detrick (MD): DOD Blast Injury Research Program Coordinating Office. Science & technology Efforts & Programs, Army Medical Research & Material Command (US); 2014. FY14 Report to the Executive Agent.
4. Kleinberger M. et al. Second workshop on numerical analysis of human and surrogate response to accelerative loading. Aberdeen Proving Ground (MD): Army Research Laboratory (US); 2016.
5. Chancey C, McEntire J, Scherer R, Frounfelker P, Tegtmeyer M. Program for Warrior Injury Assessment Manikin (WIAMan). Aberdeen Proving Ground (MD): Army Research Laboratory (US); 2011.  
[https://blastinjuryresearch.amedd.army.mil/docs/WIAMan\\_Project\\_Plan\\_Industry\\_Day\\_V3.pdf](https://blastinjuryresearch.amedd.army.mil/docs/WIAMan_Project_Plan_Industry_Day_V3.pdf).
6. Bell C, Lister K, Shirley A, Chowdhury M. Validation of a whole body WIAMan model for vehicle survivability, Ground Vehicle Survivability Training Symposium (GVSTS); 2016 Nov 5–17; Ft Benning, GA.
7. Armiger R, Boyle M, Gayzik S, Merkle M, Chowdhury M. The development of a virtual WIAMan for predicting occupant injury and vehicle performance, ground vehicle survivability training symposium (GVSTS); 2016 Nov 15–17; Ft Benning, GA.
8. Bell C, Lister K, Nohetto H, Robeck C, Yow C. User's manual and validation, WIAMan Velodyne Model – TDv1.2. Mooresville (NC): Corvid Technologies; 2016 Jun 30.
9. Vavalle N, Shanaman M, Lomicka C, Boyle M, Armiger R. User's manual and validation summary; WIAMan ATD Tech Demonstrator LS-Dyna FEM v1.0.0. Laurel (MD): Johns Hopkins Applied Physics Lab; 2016.
10. Ott K, Dooley C, Wickwire A, Iwaskiw A, Armiger R, Merkle A. Initial characterization of the human response to vertical accelerative loading. Seventh World Congress of Biomechanics; 2014 Jan 15; Boston, MA.

11. Sanborn B, Moy P, Mrozek R, Weerasooriya T. Effect of strain rates on the compressive response of neck rubber from humanetics HIII 50th percentile, male dummy under different loading sequences. Aberdeen Proving Ground (MD): Army Research Laboratory (US); 2013 Feb. Report No.: ARL-TR-6336.
12. LS-DYNA Support, Material models for polymers. Livermore (CA): Livermore Software Technology Corporation; 2016 [accessed 2016]. <http://www.dynasupport.com/howtos/material/material-models-for-polymers>.
13. LS-DYNA keyword user's manual volume II, material models (revision: 1275). Livermore (CA): Livermore Software Technology Corporation; 2012 Mar 26.
14. Jeong D, Kwok P, Canha J. Characterization of deformable materials in the THOR dummy, injury Science Research Proceeding of the 28th International Workshop; 2000 Nov; Atlanta, GA.
15. Crawford DM, Chowdhury MR, Pietsch HA. Mechanical properties of polymers used for anatomical components in the Warrior Injury Assessment Manikin (WIAMan) Technology Demonstrator. White Sands Missile Range (NM): Army Research Laboratory (US); 2016 July. Report No.: ARL-TR-7728.
16. Ogden RW. Large deformation isotropic elasticity-on the correlation of theory and experiment for incompressible rubberlike solids. Proc Royal Society of London A: Mathematical, Physical and Engineering Sciences 1972;326(1567):565–584. The Royal Society.
17. Mooney M. A theory of large elastic deformation. J Applied Physics. 1940;11(9):582–592.
18. Bower AF. Applied mechanics of solids. Boca Raton (FL): CRC press; 2009.
19. Li C, Lua J. A hyper-viscoelastic constitutive model for polyurea. Materials Lett. 2009;63(11):877–880.
20. Dakota Version 5.4 user's manual. Albuquerque (NM): Sandia National Laboratories; 2014.
21. Qi HJ, Joyce K, Boyce MC. Durometer hardness and the stress-strain behavior of elastomeric materials. Rubber Chem and Tech. 2003;76.
22. LS-DYNA keyword user's manual. Vol. II. Livermore (CA): Livermore Software Technology Corporation; 2015.

23. Bergstrom J. Mechanics of solid polymers theory and computational modeling. San Diego (CA): William Andrew; 2015.
24. Pietsch HA. et al. Evaluation of WIAMan technology demonstrator biofidelity relative to sub-injurious PMHS response in simulated under-body blast events. Stapp Car Crash J. 2016;60. Submission 16S-27,
25. PolyUMod and MCalibration software. Needham Heights (MA):Veryst Engineering; 2015.
26. Malone D. Validation and updating of the gen2 LS-DYNA model of the H-III ATD (50th percentile). UBM FY14 Task 6.1. Aberdeen Proving Ground (MD): Army Research Laboratory (US); 2014 Apr.
27. Ghere C, Gades H. Objective rating of signals using test and simulation responses. 21st Enhanced Safety of Vehicles; 2009; Stuttgart, Germany.



## List of Symbols, Abbreviations, and Acronyms

---

ARL	US Army Research Laboratory
ATD	anthropomorphic test device
BB	Bergstrom-Boyce
DAKOTA	Design Analysis Kit for Optimization and Terascale Applications
DOT&E	Director, Operational Test and Evaluation
EO	Engineering Office
FEM	finite-element model
GA	genetic algorithm
Gen	generation
JHU-APL	Johns Hopkins University Applied Physics Laboratory
LFT&E	live-fire test and evaluation
M&S	modeling and simulation
N-T UBB	Near-Term Under-body Blast
PPE	personal protective equipment
SOGA	single objective genetic algorithm
SoD	strength of design
TD	Tech Demonstrator
TTP	time to peak
UBB	under-body blast
V&V	validation and verification
VALTS	Vertically Accelerated Load Transfer System
WIAMan	Warrior Injury Assessment Manikin

1 DEFENSE TECHNICAL  
(PDF) INFORMATION CTR  
DTIC OCA

2 DIRECTOR  
(PDF) US ARMY RESEARCH LAB  
RDRL CIO L  
IMAL HRA MAIL & RECORDS  
MGMT

1 GOVT PRINTG OFC  
(PDF) A MALHOTRA

2 TARDEC  
(PDF) RDTA RS  
R SCHERER  
H PIETSCH

14 DIR USARL  
(PDF) RDRL DPW  
M CHOWDHURY  
D CRAWFORD  
F HUGHES  
J TICE  
RDRL WMM G  
J LENHART  
RDRL WMP F  
N GNIAZDOWSKI  
E FIORAVANTE  
D KRAYTERMAN  
RDRL SLB E  
C BARKER  
M MAHAFFEY  
D HOWLE  
RDRL WMP G  
S KUKUCK  
RDRL WMP B  
C HOPPEL  
T WEERASOORIYA